

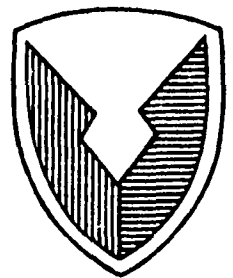
AD-A244 039



D No. _____

TECOM Project No. 7-CO-R90-DPO-004

DPG No. DPG-FR-91-701



US ARMY
MATERIEL COMMAND

METHODOLOGY INVESTIGATION

FINAL REPORT

CALIBRATION AND QUALITY CONTROL FOR
NEW METEOROLOGICAL INSTRUMENTATION, PART II

By

CHRISTOPHER A. BILTOFT

Meteorology Division
Materiel Test Directorate

U.S. ARMY DUGWAY PROVING GROUND
DUGWAY, UTAH 84022-5000

NOVEMBER 1990

Period Covered
November 1989 - September 1990

Distribution unlimited

Prepared for:
Commander, U.S. Army Test and
Evaluation command, ATTN:
AMSTE-TC-D, Aberdeen Proving
Ground, MD 21005-5055

U.S. Army Test and Evaluation
Command, Aberdeen Proving
Ground, MD 21005-5055

91-19095



91 12 26 011

Disposition Instructions

Destroy this report when no longer needed. Do not return it to the originator.

Disclaimer Statement

The views, opinions, and findings in this report are those of the author and should not be construed as an official Department of the Army position, unless so designated by other official documentation.

Trade Names Statement

The use of trade names in this document does not constitute an official endorsement or approval of the use of such commercial hardware or software. This document may not be cited for purpose of advertisement.



DEPARTMENT OF THE ARMY
HEADQUARTERS, U.S. ARMY TEST AND EVALUATION COMMAND
ABERDEEN PROVING GROUND, MARYLAND 21005-5055



REPLY TO
ATTENTION OF

23 JUL 1991

AMSTE-TC-D (70-10p)

MEMORANDUM FOR Commander, U.S. Army Dugway Proving Ground, ATTN:
STEDP-MT-M, Dugway, UT 84022-5000

SUBJECT: Methodology Investigation Final Report, Calibration and
Quality Control for New Meteorological Instrumentation, Part II,
TECOM Project No. 7-CO-R90-DPO-004

1. Subject report is approved.
2. Point of contact at this headquarters is Mr. James Piro,
AMSTE-TC-D, amstetcd@apg-9.apg.army.mil, DSN 298-2170.

FOR THE COMMANDER:

Kenneth Ballant
FREDERICK D. MABANTA
C, Technology Development Division
Directorate for Technology



Accession For	
NTIS GRA&I	<input checked="" type="checkbox"/>
DTIC TAB	<input type="checkbox"/>
Unannounced	<input type="checkbox"/>
Justification	
By	
Distribution/	
Availability Codes	
Dist	Avail and/or Special
A-1	

UNCLASSIFIED

SECURITY CLASSIFICATION OF THIS PAGE

REPORT DOCUMENTATION PAGE

Form Approved
OMB No. 0704-0138

1a. REPORT SECURITY CLASSIFICATION UNCLASSIFIED			1b. RESTRICTIVE MARKINGS		
2a. SECURITY CLASSIFICATION AUTHORITY			3. DISTRIBUTION / AVAILABILITY OF REPORT Approved for Public Release; Distribution Unlimited		
2b. DECLASSIFICATION / DOWNGRADING SCHEDULE			5. MONITORING ORGANIZATION REPORT NUMBER(S)		
4. PERFORMING ORGANIZATION REPORT NUMBER(S) DPG-FR-91-701			7a. NAME OF MONITORING ORGANIZATION		
6a. NAME OF PERFORMING ORGANIZATION U.S. Army Dugway Proving Ground		6b. OFFICE SYMBOL (if applicable) STEDP-MT-M	7b. ADDRESS (City, State, and ZIP Code)		
6c. ADDRESS (City, State, and ZIP Code) Dugway, UT 84022-5000			9. PROCUREMENT INSTRUMENT IDENTIFICATION NUMBER		
8a. NAME OF FUNDING / SPONSORING ORGANIZATION U.S. Army Test and Evaluation Command		8b. OFFICE SYMBOL (if applicable) AMSTE-TC-D	10. SOURCE OF FUNDING NUMBERS		
8c. ADDRESS (City, State, and ZIP Code) Aberdeen Proving Ground, MD 21005-5055			PROGRAM ELEMENT NO.	PROJECT / -CO- NO. R90-DP0- 004	WORK UNIT ACCESSION NO.
11. TITLE (Include Security Classification) Calibration and Quality Control for New Meteorological Instrumentation, Part II					
12. PERSONAL AUTHOR(S) Biltoft, Christopher A.					
13a. TYPE OF REPORT Methodology Report		13b. TIME COVERED FROM Oct 89 TO Sep 90	14. DATE OF REPORT (Year, Month, Day) 1990, November, 15		15. PAGE COUNT
16. SUPPLEMENTARY NOTATION					
17. COSATI CODES			18. SUBJECT TERMS (Continue on reverse if necessary and identify by block number)		
FIELD	GROUP	SUB-GROUP	Anemometer Intercomparison Testing Sodar		
04	02		Remote Sensing Doppler Acoustic Sounder Solar Radiation		
			Quality Control Radar Wind Profiler Scintillometer		
19. ABSTRACT (Continue on reverse if necessary and identify by block number) U.S. Army Dugway Proving Ground (DPG) conducted a series of tests and studies to evaluate the performance of new meteorological instrumentation. This instrumentation included Doppler acoustic sounders (sodars), crosswind scintillometers, and a radar wind profiler. An additional study was done to model the effects of solar radiation on a fiberoptic-quartz thermometer. Data collected at the International Sodar Intercomparison Experiment (ISIE) were used to develop a new methodology for testing the performance of field instruments. The scintillometer weighting function test showed that three of five weighting functions closely matched theoretical values, while two others were broader than expected. Radiation effects on a fiberoptic-quartz thermometer probe were found to be significant, and the use of a solar reflecting surface coating was recommended to minimize solar radiation effects. A radar wind profiler has been configured for maximum signal-to-noise ratio, and a study of profiler performance has been initiated with collaboration from the University of Utah Meteorology Department and the National Weather Service Western Region Headquarters.					
20. DISTRIBUTION / AVAILABILITY OF ABSTRACT <input checked="" type="checkbox"/> UNCLASSIFIED/UNLIMITED <input type="checkbox"/> SAME AS RPT <input type="checkbox"/> DTIC USERS			21. ABSTRACT SECURITY CLASSIFICATION UNCLASSIFIED		
22a. NAME OF RESPONSIBLE INDIVIDUAL Christopher A. Biltoft			22b. TELEPHONE (Include Area Code) (801)831-5101		22c. OFFICE SYMBOL STEDP-MT-M

TABLE OF CONTENTS

	<u>Page</u>
Foreword	ii

SECTION 1. SUMMARY

1.1 Background	1
1.2 Problem	1
1.3 Objectives	1
1.4 Procedures	2
1.5 Results	3
1.6 Conclusions	4
1.7 Recommendations	5

SECTION 2. DETAILS OF THE INVESTIGATION

2.1 The International Sodar Intercomparison Experiment	7
2.2 The Crosswind Scintillometer Weighting Function Test	18
2.3 Radiation Effects on a Thermometer Probe	30
2.4 Radar Wind Profiler Performance Optimization	40

SECTION 3. APPENDICES

A. Methodology Investigation Proposal and Directive	A-1
B. References	B-1

FOREWORD

This project was supported by FY90 Research, Development, Test, and Evaluation (RDTE) Methodology Funds. The study was performed by the Meteorology Division, Materiel Test Directorate, U.S. Army Dugway Proving Ground. Data for the International Sodar Intercomparison Experiment (ISIE) were provided by Dr. Bruce Baker of the U.S. Environmental Protection Agency (EPA) Research Triangle Park Office. Statistical procedures used in the ISIE portion of this report were reviewed by Mr. Cecil Eckard of Andtulis Research Corporation. Mr. James Osterud of the Dugway Instrumentation Branch collected data for the Crosswind Scintillometer Weighting Function Test. Mrs. Susan Gross provided word processing support during report preparation.

SECTION 1. SUMMARY

1.1 BACKGROUND

U.S. Army Dugway Proving Ground (DPG) is completing a modernization program that has included upgrading meteorological measurement capabilities. A number of new instruments have been acquired or developed that provide measurement capabilities unavailable with older instrument designs. Some of these systems, such as the Doppler acoustic sounder (sodar) and radar wind profiler, utilize energy backscattered from density discontinuities in the atmosphere to measure vertical profiles of wind and turbulence. Another remote sensing instrument, the spatially-averaged filter scintillometer, is a forward-scatter wind component and turbulence measurement device with a transmitter and down-range receiver. Other instruments such as the sonic anemometer and quartz crystal-fiberoptic thermometer are designed for in-situ measurements. Each of these instruments has unique methodology development requirements related to performance evaluation.

This Part II study reports on the FY90 DPG effort to develop methodologies for evaluating the performance of new meteorological instrumentation. These efforts are significant because of the increased demands for the specification of atmospheric effects on the performance of multispectral target acquisition systems, smokes/obscurants, and munitions delivery systems. Included in this report are results of the International Sodar Intercomparison Experiment (ISIE), a scintillometer weighting function test, a study of radiation effects on a thermometer probe, and the initial phase of a radar wind profiler performance evaluation study. The ISIE was conducted at the Boulder Atmospheric Observatory (BAO) in association with representatives of the National Oceanic and Atmospheric Administration (NOAA) Environmental Research Laboratories/Wave Propagation Laboratory (ERL/WPL), U.S. Environmental Protection Agency (EPA), and White Sands Missile Range as well as participants from France and Japan. The scintillometer weighting function test and the thermometer probe radiation study were performed at DPG with in-house resources. The ongoing radar wind profiler evaluation includes participants from the National Weather Service Western Region Headquarters in Salt Lake City and the University of Utah Meteorology Department.

1.2 PROBLEM

The advent of new meteorological instrumentation requires the development of new methodologies to evaluate instrument performance, as well as new procedures for processing and interpreting data. Remote sensing instruments do not lend themselves to laboratory calibrations or the laboratory-derived transfer functions used for standard meteorological instrumentation. Consequently, evaluation procedures based on field inter-instrument comparisons are needed.

1.3 OBJECTIVES

The objectives of this study were to develop a methodology for characterizing the performance of new meteorological instruments, define procedures for optimizing their operation, and develop improved test data reduction and analysis procedures.

1.4 PROCEDURES

This Part II study included methodology development for four different instruments: Doppler acoustic sounders (sodars), the spatially-averaged filter scintillometer, a quartz crystal-fiberoptic thermometer, and the radar wind profiler. Methodologies were developed for defining sodar performance, evaluating scintillometer weighting functions, and calculating radiation effects on thermometers. An additional study was initiated to optimize the radar wind profiler's signal prior to the evaluation of its performance.

Sodars are ground-based remote sensing instruments that use the Doppler effect with acoustic energy backscattered from clear air turbulence elements as a means of measuring profiles of wind and turbulence within the planetary boundary layer. Because these instruments are large and operate in the open air, sodar performance must be evaluated through a series of intercomparison tests using data from multiple instruments for reference. DPG participated in the ISIE conducted during September 1988 at the BAO in order to obtain a data set that could be used to develop a sodar performance evaluation methodology. Three sodars of the types used at DPG were operated in proximity to each other during the ISIE. The ensuing data set was used to develop a methodology for sodar performance evaluation.

The methodology selected for sodar performance evaluation is based on the precision estimation techniques developed by Grubbs (1948) and contained in DARCOM Pamphlet 706-103. The principal figure of merit is relative precision, which is defined by Thompson (1963) as the ratio of the instrument's measurement precision to the variability in the quantity measured. This methodology is based on the premise that the required measurement precision is a function of the variability of the quantity to be measured. A relative precision of 3 or greater is tentatively defined as adequate for general meteorological purposes. An experimental procedure to define independent sample size is also introduced and used with statistical significance tests.

The crosswind scintillometer consists of a transmitter aligned with a receiver located approximately 1 km downrange along a line-of-sight optical path. The transmitter uses a light emitting diode (LED) source radiating over Fresnel lenses, and the receiver optics contains another set of Fresnel lenses. Combinations of filters on the transmitter and receiver form peaks in the received signal weighting functions at five positions along the optical path, providing simultaneous crosswind component measurements at five segments along the optical path. The positions of the weighting functions are derived from theoretical calculations based on the work of Lee (1974). Verification of the weighting functions in the ambient air is difficult because the winds at any one position along the optical path are strongly correlated with the winds at other positions along the path. Consequently, a helicopter was used to create rotor wash that perturbed the wind field. By flying slowly along a path parallel to the optical path, the helicopter was able to create a localized wind field that was not correlated with winds at other segments along the path. Concurrent measurements were made using sonic anemometers as a reference for scintillometer path segment crosswind measurements.

TACAN Corporation is developing a quartz crystal-fiberoptic thermometer for micrometeorological applications in a Phase II Small Business Innovative Research (SBIR) effort for which DPG is the Army project manager. This

development combines the inherent precision of quartz crystal temperature measurement technology with the advantages of fiberoptic data transmission in an effort to develop an accurate thermometer for field applications. A major concern for accurate open air thermometry is the effect of solar heating on the thermometer probe. The Luers (1990) heat balance model was used to evaluate these radiation effects.

DPG has recently acquired a 5-beam 404-MHz pulsed Doppler radar designed to measure vertical profiles of wind from 500 m to 12 km or more above ground level. The radar wind profiler is a fixed installation located near DPG's West Vertical Grid. It's 5-beam configuration allows a great deal of flexibility in the evaluation of profiler performance because the east and west beam measurements can be intercompared, as can the north and south beam measurements. To facilitate intercomparison, the profiler has been configured to operate as two collocated 3-beam profilers. Initial checks are being performed on the returned power, spectral width, and noise level. Profiler settings are being adjusted to maximize returned power prior to initiation of performance evaluation. Profiler performance evaluation will include intra-profiler comparisons using the dual 3-beam configurations and intercomparisons between the profiler winds and wind measurements obtained from nearby radiosonde and tethered flights. Members of the National Weather Service Western Region Headquarters and the University of Utah Meteorology Department have agreed to participate in the profiler evaluation.

1.5 RESULTS

The data set collected at the ISIE was of sufficient quality to use relative precision as a figure of merit for inter-sodar performance evaluations. The AeroVironment, DPG, and White Sands Missile Range sodars exhibited relative precisions in excess of 3 for horizontal wind component measurements, which is considered satisfactory for general meteorological applications. Consequently, sodar 20-min wind readings were found to be sufficiently precise for most applications. The DPG and AeroVironment sodars also exhibited marginal (~3) relative precisions in their measurements of vertical velocity variance. None of the 20-min averaged sodar data exhibited adequate relative precision for horizontal wind angle standard deviation or mean vertical velocity measurements. Sodar wind measurements were found to be further limited at high wind speeds. High wind speeds degrade sodar performance by increasing background noise and by deflecting the acoustic beams away from the receiving antennas. The ISIE data show that sodar wind measurements are unlikely to be reliable for wind speeds in excess of 14 m s^{-1} . The common-volume horn configuration in which the DPG sodar was deployed at the ISIE provided no measureable improvement in sodar performance over the standard trailer-mounted configuration. These results suggest that the compact trailer-mounted configuration that optimizes sodar mobility does not seriously compromise data quality.

The scintillometer weighting function test indicated that the mid-path weighting function is well isolated, while the 1/3 and 2/3 path segment weighting functions appear to contain contributions from other portions of the optical path. These results were sent to the contractor (Scientific Technologies, Inc.) working on an advanced spatially-averaged filter scintillometer prototype in a Phase II SBIR effort for which DPG is the Army project manager. Follow-on testing of the advanced scintillometer prototype will include similar weighting function tests. However, future tests will use a technique that

generates lower wind speeds and turbulence intensities than the helicopter because the rotor wash created so much turbulence that scintillometer operating assumptions were violated and one sonic anemometer mast was blown over.

The thermometer radiation study revealed that temperature biases of several tenths of a degree Celsius can occur under strong radiation conditions even when a small sensor is used. The use of various solar reflecting coatings on the sensor is being explored to alleviate this problem. Also, algorithms will be developed to use supplemental wind and solar radiation measurements for removal of the solar heating measurement bias. Field testing of the new fiber-optic-quartz thermometer has begun, and will include tests of sensors with newly developed solar reflecting surfaces.

The radar wind profiler was configured to operate as two collocated 3-beam profilers. An intercomparison of the resulting data indicated that the received power from the x-axis beam is several decibels lower than the y-beam power. The difference was found to be statistically significant. Some statistically significant differences were also found in the east versus west and north versus south beams. These results were discussed with the manufacturer (Tycho Technologies, Inc.), who made some adjustments in the antenna. The relative precision methodology developed for ISIE sodar evaluation will be used to evaluate profiler performance following further testing of profiler radar configurations and data reduction algorithms.

1.6 CONCLUSIONS

Statistical techniques presented in DARCOM Pamphlet 706-103 have been adopted for evaluating the performance of meteorological instrumentation. These techniques were successfully used to evaluate sodar performance during the ISIE. Analyses of the data by DPG and other ISIE participants indicate that sodars can provide useful wind profile measurements from approximately 50 to 700 m above ground level. This remote sensing instrument is therefore a mobile and economical method for making wind measurements beyond the height range of most meteorological towers. However, sodar data must be treated with caution for high wind speed conditions. Good results require careful attention to equipment set-up, operation, maintenance, and data analysis. Sodars also have a marginal capability for measuring vertical velocity variance, but little or no capability for reliable measurements of the mean vertical velocity or horizontal wind angle standard deviation when averaging periods on the order of 20 min are used. There is also little utility in dismounting sodar horns to achieve a common-volume configuration.

The theoretical spatially-averaged filter scintillometer weighting functions are approximately correct, although several of them are broader than predicted by theory. These scintillometers can provide simultaneous measurements of cross-path wind components at multiple positions along a 1-km optical path. Problems identified during the DPG scintillometer weighting function test should lead to improvements in the advanced prototype scintillometer under development as a Phase II SBIR effort.

Solar radiation can create a temperature measurement bias of several tenths of a degree Celsius even with sensors of small size and negligible thermal mass. The results of this study should lead to the use of optical solar

reflecting coatings on the quartz crystal-fiberoptic thermometer currently under development as a Phase II SBIR effort.

Differences in received power have been identified for the various beam configurations of the DPG radar wind profiler. This information has led to the replacement of some antenna components and to an optimization of the profiler's operating configuration. Further testing will include intra-profiler comparisons and comparison of profiler-derived wind profiles with profiles obtained from radiosonde and tethered flights.

1.7 RECOMMENDATIONS

The experimental statistical techniques presented in DARCOM Pamphlet 706-103 and applied to the ISIE sodar data are likely to have wide applications for intercomparison testing of meteorological instruments in the field, and may be applicable to the testing of other complex instrument systems as well. However, some limitations of currently available techniques must first be overcome. These limitations include the lack of a significance test for relative precision using three or more instruments and the absence of a procedure for adjusting sample size when statistically independent sampling is impractical. A technique for estimating the independent sample size from the ISIE data set is included in Section 2.1 of this report. The validity of this technique and its application to significance testing should be evaluated prior to adoption into instrumentation evaluation methodologies. The development of a significance test for relative precision and validation of the new sample size estimation technique could be addressed by theoretical statisticians through the Army Research Office.

INTENTIONALLY BLANK

SECTION 2. DETAILS OF THE INVESTIGATION

2.1 THE INTERNATIONAL SODAR INTERCOMPARISON EXPERIMENT

2.1.1. Background

Monostatic Doppler acoustic sounders (sodars) are ground-based remote sensing instruments that use the Doppler effect with acoustic pulses to measure wind and turbulence profiles from 50 to 500 - 1000 m above the sodar antenna array. The most common sodar configuration includes a 3-antenna array mounted on a trailer, with one antenna transmitting acoustic energy directly above the array (the vertical axis) and the other antennas tilted 15 to 18 degrees off axis towards the north or south and east or west. This arrangement permits wind measurements made along the antenna radial directions to be resolved into the vertical, north-south, and east-west wind components. These wind components are then converted into wind speed, wind direction, and turbulence data.

Sodars utilize the Doppler shift of backscattered acoustic energy as a means of obtaining wind and turbulence measurements. A measurement cycle begins with the transmission of acoustic pulses from compression drivers within one of the tuned directional antennas. After transmitting, each antenna sits for a few seconds in a listening mode to receive backscattered signals. The transmitted acoustic energy propagating along a radial direction encounters thermal inhomogeneities in the atmosphere which scatter the energy, a small portion of which is backscattered towards the antenna of origin. Each return signal is characterized by its intensity, Doppler frequency shift, and spectral width. The arrival of each signal is also time-tagged. The time interval between transmission and reception, multiplied by the speed of sound and divided by two (to account for the round trip out from and back to the antenna), identifies the radial distance at which the scattering occurred. The Doppler shift in the return signal's acoustic frequency indicates the speed and direction of air motion along the radial axis; the frequency is shifted towards a higher frequency if the scattering volume is moving toward the antenna, and towards a lower frequency if the scattering volume is moving away from the antenna. Signal processing techniques are used to assess data quality and remove noise. Additional software converts the returned signals into vertical profiles of wind and turbulence.

Sodar performance is a function of transmitted pulse energy, antenna gain, acoustic frequency, pulse repetition frequency, ambient noise, and atmospheric conditions. Consequently, sodar performance can vary dramatically from site to site or from day to day at a given site. A series of intercomparison tests have been performed in recent years in an attempt to characterize sodar performance. The most recent of these tests, the International Sodar Intercomparison Experiment (ISIE), was conducted at the Boulder Atmospheric Observatory (BAO) near Boulder, Colorado from 29 August to 18 September 1988. The ISIE provided sets of simultaneous measurements by commercially-available sodars that can be used for intercomparison against each other, or against measurements made on the 300-m BAO tower. The BAO tower is instrumented with sonic anemometers and propeller-vane wind equipment as described by Kaimal and Gaynor (1983), and has been used as a "de facto" reference for intercomparison experiments.

2.1.2. Test Design

The primary objective of DPG participation in the ISIE was to collect a comprehensive data set that could be used to develop a methodology for evaluating sodar performance. An additional objective for the DPG sodar was to evaluate the effect of volume separation on sodar performance. Sodar performance concerns included its wind, vertical velocity, and turbulence measurement capabilities and its performance in high wind conditions.

DPG's participation in the ISIE, which was partially funded by FY88 quick reaction methodology funds, was particularly advantageous because it provided an opportunity to intercompare data from the three types of sodars used at DPG: the AeroVironment system operating at 1497 Hz provided by AeroVironment, Inc., a Remtech system operating at 1600 Hz provided by the White Sands Missile Range, and a Remtech system operating at 2400 Hz provided by DPG. Additional sodars participating in the ISIE are shown on Figure 1. The three sodars evaluated in this study were situated 300 to 500 m south of the BAO tower and were separated from each other by a maximum of 300 m. With the exception of the DPG unit, all of the participating sodars were mounted on trailers. Trailer-mounted sodars designed to resolve horizontal wind components necessarily have each horn oriented towards a different wind direction component. Although this arrangement causes increasing beam separation as a function of height, it must be assumed for data reduction purposes that the volume of air sampled within each beam is an independent realization of the same turbulent process and that sample differences can be resolved through temporal averaging. The DPG unit was dismounted and placed in a triangular configuration so that the beams propagating from the off-vertical horns converged towards the vertical beam. With a spacing of 42 m, this configuration minimized sampling volume separation, providing a common measuring volume at 150 m above ground level. Inter-sodar performance evaluations described in this report were conducted with data collected at the 150-m level.

Meteorological variables measured during the ISIE included wind speed (\bar{U}), wind direction ($\bar{\theta}$), wind direction standard deviation (σ_{θ}), vertical wind velocity (\bar{w}), and vertical velocity standard deviation (σ_w). For each of the variables, the set of simultaneous measurements by all three sodars was used as a basic unit of analysis (case). Because of the difficulties involved in analyzing vector winds, the mean wind speed and direction measurements were decomposed into easting (\bar{E}) and northing (\bar{N}) components for case analysis.

Data from all participating sodars and the BAO tower instruments were compiled into a common format by Dr. Bruce Baker of the U.S. Environmental Protection Agency, and the formatted data sets were subsequently distributed to participants for analysis. The basic data averaging period was 20 min, and a sample was taken every time data from all three sodars were available.

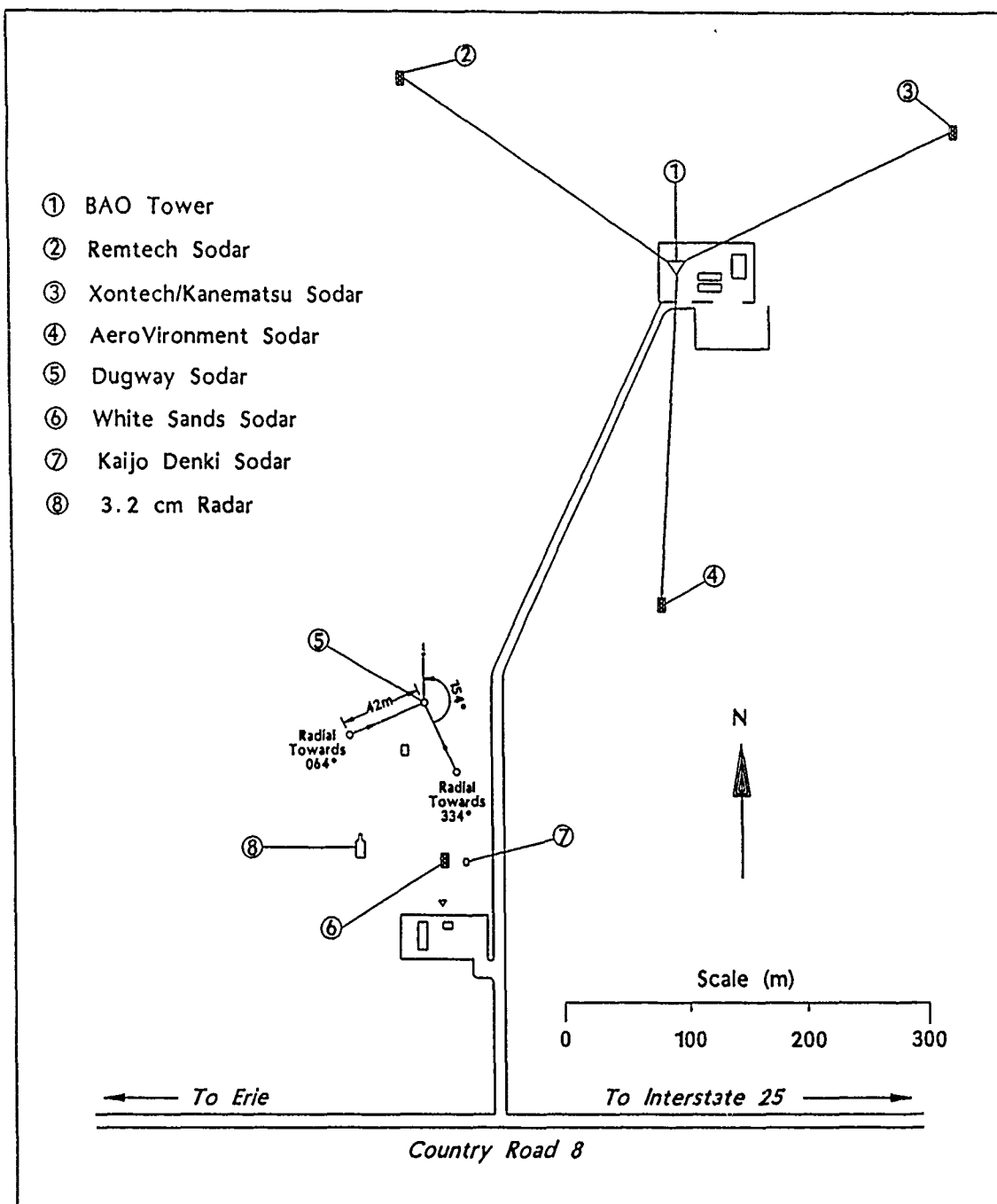


Figure 1. The Instrumentation Layout at the BAO During the ISIE Showing the Sodar and Radar Positions Relative to the BAO Tower.

2.1.3. Precision and Significance Test Methodologies

Sodar performance can be described in terms of bias and precision. Because sodars are remote sensing instruments, measurement bias due to factors such as miscalibration, hysteresis, and sensor age is largely absent. Measurement bias due to instrument misalignment, data processing errors, or faults in the grounding, cabling, or electronics is possible, but the occurrence of these kinds of errors is a function of the care with which the sodar is set up, operated, and maintained. Consequently, measurement precision, rather than bias, is the major concern in the development of a methodology for evaluating sodar performance.

The methodology selected for sodar evaluation is an outgrowth of the procedures developed by Grubbs (1948) for estimating the precision and product variability of two or more measuring instruments. Separate estimates of instrument precision and the variability of the quantity being measured are obtained for each case using this methodology. The ratio of these two estimated quantities is defined as the relative precision (Thompson, 1963). Relative precision provides a quantitative evaluation of an instrument's measurement precision with respect to the variability of the measured quantity. Precision determinations are followed in the methodology by a significance test developed by Grubbs (1973) that is used to evaluate inter-instrument variances in errors of measurement, as presented in DARCOM Pamphlet 706-103. However, before applying significance test procedures, a technique based on information contained in Brooks and Carruthers (1953) is used to quantify the degree of independence between 20-min averaged samples within the data sets and to correct the sample size to the number of "independent" samples. Significance tests are performed using this corrected number of independent samples.

Concurrent data from the DPG, White Sands Missile Range (WS), and Aero-Vironment (AV) sodars constituted the samples used in the 3-instrument precision tests for \bar{E} and \bar{N} as well as σ_w and σ_θ . A two-way precision estimate of \bar{w} was obtained using only the DPG and WS sodars because of uncertainties in the AV vertical velocity measurements. The precision tests were followed by significance tests of the results. Pertinent variates for three-way precision computation were the sample variances of the differences in readings between the WS and AV sodars (S_a^2), the DPG and WS sodars (S_b^2), and the DPG and AV sodars (S_c^2). If the instrumental errors are uncorrelated, maximum likelihood estimates^c of the sodar standard errors of measurement ($est\sigma_1$, $est\sigma_2$, and $est\sigma_3$ for the AV, WS, and DPG sodars, respectively) are (Grubbs, 1948)

$$est\sigma_1 = ((S_a^2 - S_b^2 + S_c^2)/2)^{0.5} \quad (1)$$

$$est\sigma_2 = ((S_a^2 + S_b^2 - S_c^2)/2)^{0.5} \quad (2)$$

$$est\sigma_3 = ((-S_a^2 + S_b^2 + S_c^2)/2)^{0.5} \quad (3)$$

For the two-instrument intercomparisons, estimates of the instrumental errors are given by

$$est\sigma_1 = (S_1^2 - S_{12})^{0.5} \quad (4)$$

$$\text{est}\sigma_2 = (S_2^2 - S_{12})^{0.5} \quad (5)$$

where S_1^2 and S_2^2 are the sample variances of the readings by the WS and DPG sodars, and S_{12} is the covariance of readings between the two instruments. This covariance is obtained using the sample variance S_{1-2}^2 of the differences in paired readings between the two instruments under the assumption that its subtraction from the sum of the variances leaves only the error differences as a residual. That is, S_{12} is assumed to be given by

$$S_{12} = [(S_1^2 + S_2^2) - S_{1-2}^2]/2 \quad (6)$$

Equations (1) through (6) consider only the differences in measurement biases and random measurement errors for the instrument pairs. Consequently, these equations are applicable to the ISIE sodar data only if the independent realizations of the turbulent processes measured by each sodar included no systematic differences and no correlated measurement errors. Temporal averaging over a 20-min period should have minimized measurement differences due to spatial separations on the order of several hundred meters. (This assumption has been used with apparent success during previous tests at the BAO tower.) Each sodar used different hardware and software. These differences minimized the possibility of statistically dependent inter-instrument errors. The possibility that sodar performance degradation at high wind speeds resulted in error correlations is considered later in this report. Rational physical bases for other possible correlations between instrument errors and measured variables have not been identified. Therefore, it is unlikely that the assumptions of Equations (1) through (6) were seriously violated except possibly during infrequent periods with high wind speeds.

Grubbs (1948) provides a method for estimating the population variance of the measured atmospheric variable ($\text{est}\sigma_x^2$). This estimate, which is equivalent to the average of the covariances of the readings of the three instruments, is given as

$$\text{est}\sigma_x^2 = (S_{r+s+t}^2 - \{S_a^2 + S_b^2 + S_c^2\}/2)/9 \quad (7)$$

where S_{r+s+t}^2 is the sample variance of the sum of the three instrument readings. Sodar relative measurement precision for each case is then obtained as a ratio of $\text{est}\sigma_x$ to $\text{est}\sigma_i$, where i has values of 1, 2, or 3 for each of the three instruments. Thompson (1963) cites a relative precision on the order of 10 as a "rule of thumb" for precise measurement. At the other extreme, a ratio of 1.0 or less would characterize an instrument of such imprecision that major changes in the measured variable would be missed. For atmospheric measurements, a relative precision between 3 and 10 is likely to be adequate for most applications. Relative precisions were calculated for each case using the ISIE sodar measurements of vertical velocity, vertical velocity variance, horizontal wind angle standard deviation, and easting and northing wind components. The results are presented in the following subsection.

2.1.4. Results

Table 1 lists the variances of the meteorological variables comprising each case for the WS, AV, and DPG sodars, as well as the variances of the inter-instrument differences. The /y vertical wind component data were not used because of uncertainties about whether a zero reading was due to a zero vertical velocity or the absence of data. The S_D^2 column in Table 1 presents the variances of the DPG data sets for each case. Variances for the AV and WS data sets are identified in the table as S_A^2 and S_W^2 , respectively. The inter-instrument differences and sample sizes are also included in the table.

Table 1. Sample Variances of Measurements from the WS, AV, and DPG Sodars; Variances of the Inter-Instrument Differences; and Sample Size.

Case	Units	S_W^2	S_A^2	S_D^2	S_a^2	S_b^2	S_c^2	M^a
\bar{E}	$m^2 s^{-2}$	15.721	15.740	12.189	1.507	1.277	1.634	148
\bar{N}	$m^2 s^{-2}$	8.248	9.947	8.389	0.881	1.146	1.349	148
\bar{W}	$m^2 s^{-2}$	0.066	--- ^b	0.056	---	0.055	---	163
σ_W^2	$m^2 s^{-2}$	0.061	0.081	0.048	0.024	0.024	0.012	158
σ_θ^2	deg^2	241.1	125.6	276.9	178.1	308.1	250.7	128

^aNumber of 20-min averages in the data set.

^bNot Available.

The results of the sodar intercomparisons are summarized in Tables 2 and 3. Table 2 presents estimates of the variance in errors of measurement for the WS (σ_1^2), AV (σ_2^2), and DPG (σ_3^2) sodars and an estimate of the variance of the measured atmospheric variable (σ_x^2) for each case. Table 3 shows the relative precision of measurements made by the WS, AV, and DPG sodars for each case. If a relative precision of 3 or better is used as the criterion for a useful meteorological measurement, all three sodars were successful in measuring mean wind components, and the AV and DPG sodars exhibited a marginal capability for σ_W measurement. The relative precisions for all other cases presented in Table 3 are well below 3.

Table 2. Estimates of the Variances in Errors of Measurement for the AV, WS, and DPG Sodars and Estimates of the Variances of the Measured Variables for Each Case.

Case	Variance Units	σ_1^2	σ_2^2	σ_3^2	σ_x^2
\bar{E}	$m^2 s^{-2}$	0.932	0.575	0.702	13.814
\bar{N}	$m^2 s^{-2}$	0.542	0.339	0.807	8.298
\bar{w}	$m^2 s^{-2}$	---	0.023	0.032	0.033
σ_w^2	$m^2 s^{-2}$	0.006	0.017	0.007	0.058
σ_θ^2	deg^2	60.38	117.71	194.34	77.00

^aNot Available.

Table 3. Relative Precision of Measurements Made by the AV, WS, and DPG Sodars.

Case	σ_x/σ_1	σ_x/σ_2	σ_x/σ_3
\bar{E}	3.8	4.9	4.4
\bar{N}	3.9	4.9	3.2
\bar{w}	--- ^a	1.2	1.0
σ_w	3.0	1.8	2.9
σ_θ	1.1	0.8	0.6

^aNot Available.

In order to perform statistical significance tests, it is necessary to determine the number of independent samples within the data set. The ISIE data set contains some data from consecutive 20-min sampling periods. These data are not entirely independent because a certain degree of persistence exists in the wind and turbulence fields over periods longer than 20 min. Therefore, the number of truly independent samples (m) is less than M . This problem is discussed by Brooks and Carruthers (1953), who provide, as a measure of persistence in time-dependent meteorological data, a persistence factor defined as

$$R_a = \frac{\sigma\sqrt{2}}{\sigma_d} - 1 \quad (8)$$

where σ is the standard deviation of a data set and σ_d is the standard deviation of the differences obtained from one observation to the next within the data set. If the data are in a random series (i.e., no persistence from one time period to the next), σ_d should approach $\sigma\sqrt{2}$ and R_a should approach zero. To obtain an estimate of the independent sample size, M was divided by $|R_a| + 1$, where $|R_a|$ denotes the absolute value of R_a . The persistence factor, original sample size, and the estimated number of independent samples for each case and each sodar are presented in Table 4. The persistence factors in the table are relatively large for easting, northing, and σ_w measurements, but are much smaller for \bar{w} and σ_θ measurements where the data include a large noise component. The data in Table 4 also show that the independent sample size can be considerably smaller than the original sample size when meteorological data are collected over consecutive time periods.

Table 4. Persistence Factor R_a , Original Sample Size M , and Number of Independent Samples \bar{m} for ISIE Data Collected by the WS, AV, and DPG Sodars.

Case	R_a			M			\bar{m}		
	WS	AV	DPG	WS	AV	DPG	WS	AV	DPG
\bar{E}	1.476	1.865	1.895	148	148	148	60	52	51
\bar{N}	1.644	1.811	1.363	148	148	148	56	53	63
\bar{w}	0.265	--- ^a	0.294	163	---	163	129	---	126
σ_w	0.828	1.275	1.381	158	158	158	86	69	66
σ_θ	0.018	0.248	0.259	128	128	128	126	103	102

^aNot Available.

Independent sample size estimates from Table 4 were used for significance tests on the ISIE data. While the use of \bar{m} with a t-statistic must be considered an experimental procedure awaiting rigorous proof, the only available alternatives are to use M (known to be an overestimate of independent sample size) or to perform no significance tests. A test using the null hypothesis that the relative precision is greater than or equal to a specific figure ($\sigma_x/\sigma_{ei} \geq 3$, for example) would be most useful. Unfortunately, a 3-instrument

significance test for relative precision has not been found in available reference material. Another useful test evaluates the null hypothesis that inter-instrument measurement precisions are equal (i.e., $\sigma_i = \sigma_j$, where i and j are alternatively 1, 2, or 3). Grubbs (1973) provides a significance test for this hypothesis.

Following Grubbs (1973), a t-statistic can be computed for selected σ_i and σ_j . The appropriate statistic for $i=1$ and $j=2$ (the WS and AV sodars) based on Student's t is

$$t(m-2, \sigma_1 = \sigma_2) = \frac{[(S_w^2/S_A^2) - \phi] (m-2)^{1/2}}{[4\phi(1-r_{bc}^2) (S_w^2/S_A^2)]^{1/2}} \quad (9)$$

where ϕ , a ratio of expected values of variances defined by

$$\phi = (\sigma_2^2 + \sigma_3^2) / (\sigma_1^2 + \sigma_3^2) , \quad (10)$$

assumes a numerical value of 1.0. The correlation coefficient in the denominator of Equation (9) defines a correlation between a pair of inter-instrument differences. For example, the inter-instrument differences AV-DPG and DPG-WS were used to obtain r_{bc} . Through appropriate changes in the subscripts of Equation (9) variables, variances of the inter-instrument differences presented in Table 1 were used to evaluate the null hypotheses $\sigma_1 = \sigma_2$, $\sigma_2 = \sigma_3$, and $\sigma_3 = \sigma_1$ for the variances in errors of measurement presented in Table 2.

Statistics generated from Equation (9) were compared with the Student's t distribution to test the null hypotheses $\sigma_i = \sigma_j$ at the 5 percent level of significance (one-tail test). This level of significance provides 1 chance in 20 that the null hypothesis would be rejected when actually true. Tests were conducted using the smallest of the pertinent independent sample sizes obtained from Table 4.

The null hypotheses were not rejected for all $\sigma_i = \sigma_j$ obtained for the \bar{E} and \bar{N} cases except for the WS versus DPG \bar{N} , where the measurement precision was found to be significantly less for the DPG sodar. This result suggests that the DPG sodar measurements contained more scatter (noise) than the WS sodar measurements, although all sodars performed at an acceptable level with relative precisions greater than 3.0. For the σ_w case, the null hypothesis was rejected for both $\sigma_1 = \sigma_2$ and $\sigma_2 = \sigma_3$, leaving the alternative that σ_2 is significantly greater than σ_1 and σ_3 . The $\sigma_1 = \sigma_3$ hypothesis was not rejected for this case. These test results, combined with a relative precision below 3.0, indicate a deficiency in the WS sodar σ_w computation algorithm. Significance tests for the σ_θ case revealed no significant differences between the AV and WS σ_θ measurements, but the DPG measurement precision was significantly less than the other two. However, relative precisions for all measurements were well below 3.0, so none of the σ_θ were considered useful.

Significance testing for \bar{w} was different from the other cases because only the WS and DPG data were used. DARCOM Pamphlet 706-103 provides a 2-instrument significance test of $\sigma_2 = \sigma_3$ based on the sample correlation and the Student's t

test. The null hypothesis $\sigma_2 = \sigma_3$ was rejected at the 95 percent level, leaving the alternative that a significant difference exists between the WS and DPG sodar vertical velocity measurement precisions. However, the relative precision of both were well below 3.0, indicating that neither set was usable. A summary of significance test results for the inter-instrument measurement precisions is presented in Table 5.

Table 5. Summary of Inter-Sodar Measurement Precision Tests.

Case	Measurement Precision $H_0: \sigma_i = \sigma_j$		
	WS=AV	WS=DPG	AV=DPG
\bar{E}	Accept	Accept	Accept
\bar{N}	Accept	Accept	Reject
\bar{w}	----- ^a	Reject	-----
σ_w	Reject	Reject	Accept
σ_θ	Accept	Reject	Reject

^aNot Available.

A follow-on test was performed to examine the relationships between the averages of the sodar wind components and the wind components derived from the BAO tower. The figure of merit used in this comparison was the linear correlation coefficient (r). The inter-sodar correlation coefficients and the correlation coefficients between the averages of the sodar wind components and the corresponding values from the BAO tower are presented in Table 6. Although the inter-sodar correlation coefficients are 0.92 or greater, the correlations of sodar averages with the tower are 0.77 and 0.84 for the easting and northing cases, respectively. The lower sodar-tower correlations suggest that the measured winds at the sodar locations contained occasional systematic differences from measured winds at the BAO tower. The ISIE data set was subsequently examined to identify several cases where these apparent differences occurred.

Several examples were found within the ISIE data set of differences between the BAO tower and averaged sodar measurements. One example occurred with very high wind conditions during the period 1520 to 1600 UCT on 10 September 1988. The wind speed measured by the tower-mounted prop-vane increased from 6.4 to 18.5 m s⁻¹ during this period, but the sodar wind measurements did not follow suit. A likely physical explanation is that the sodars were unable to operate reliably in these strong wind conditions. A second example of large sodar-BAO tower measurement differences occurred on 14 September between 1900 and 2100 UCT. The BAO tower prop-vane and sonic anemometer wind directions were consistently from the northwest, while winds measured by all three sodars were consistently from the northeast. It is unlikely that these differences are due to simultaneous malfunctions. The most likely explanation appears to

be an actual difference in the wind direction between the tower and sodar sites. A third example of interest occurred on 18 September between 0120 and 0600 UCT. In this example, winds were shifting from east-northeast through north to southwest. This transition occurred more rapidly at the sodar sites than at the BAO tower, resulting in a large apparent wind shear between the sodar sites and the tower.

Table 6. Wind Easting and Northing Component Correlation Coefficients Between the DPG, WS, and AV Sodars and Between the 3-Sodar Average (SOD) and BAO Tower Measurements.

Case	DPG-WS	DPG-AV	WS-AV	M ^a	SOD-BAO	M ^a
\bar{E}	0.95	0.96	0.95	148	0.77	146
\bar{N}	0.92	0.94	0.96	148	0.84	146

^aSample Size.

2.1.5. Conclusions

The ISIE data set was of sufficient size and quality to permit the development of a methodology for sodar performance evaluation. The key figure of merit used for sodar performance was relative precision: the square root of the ratio of the estimated variance in the variable of interest to the estimated variance of the measurement errors. An experimental technique for obtaining independent sample size estimates was also introduced. These sample size estimates were used with t-statistics to evaluate inter-instrument measurement precisions, revealing significant inter-instrument differences. This combination of techniques appears to constitute a reasonable methodology for evaluating instrument performance through intercomparison testing, but the underlying statistical theory requires development.

A relative precision of 3 or better is considered satisfactory for general meteorological measurements. Because the AV, DPG, and WS sodars exhibited a relative precision in excess of 3 for horizontal wind component measurements, these sodars are considered adequate for 20-min averaged mean wind measurements. The DPG and AV sodars also exhibited marginal (~3) relative precision for σ_w measurement. None of the 20-min averaged sodar measurements provided adequate relative precision for measurement of σ_θ or \bar{w} . The slow sampling rates and lack of coherent averaging are the likely reasons for the deficiencies in turbulence and vertical velocity measurement capabilities.

Sodar wind measurement capabilities are further limited at high wind speeds. High wind speeds generate increased background noise and deflect the acoustic beams away from the receiving antennas. Based on the limited number of high wind speed cases available, sodar performance appears to be severely degraded for wind speeds in excess of 14 m s^{-1} . Under these conditions, the assumption that instrument errors are uncorrelated with each other appears to

be violated because all three sodars suffer similar degradation. The ISIE data set did not contain a sufficient number of high wind speed cases to perform tests of statistical significance for this condition.

The common-volume configuration used with the DPG sodar produced no discernable improvement in performance over the standard trailer-mounted configuration used with the WS and AV sodars. This arrangement was tested only for the 150-m level. Although a different result is possible at higher levels where sampling volume separations are greater, the results of the present study do not justify any move to abandon the more compact trailer-mounted sodar configuration.

Analysis showed that the wind readings from the three sodars were more strongly correlated with each other than were the averages of their readings with the BAO tower wind measurements. A major premise of previous BAO tower tests has been that horizontal homogeneity exists over the area surrounding the BAO tower for averaging periods of 20 min. The ISIE test results demonstrate that this is not always the case. The most likely physical explanation is that subtle terrain differences sometimes create persistent wind shear zones. These effects must be carefully considered during instrument site selection, or when measurements made at one site are applied elsewhere.

2.2 THE CROSSWIND SCINTILLOMETER WEIGHTING FUNCTION TEST

2.2.1. Introduction

Crosswind profiling scintillometers are remote sensing instruments that use spatial filters in a forward scatter, continuous wave technique to obtain cross-path wind component measurements at segments along an optical path. The optical path is established between the scintillometer transmitter and its downrange receiver, with typical pathlengths on the order of a kilometer. Two prototype crosswind scintillometers were built for DPG by the National Oceanic and Atmospheric Administration (NOAA) Environmental Research Laboratories/Wave Propagation Laboratory (ERL/WPL). These instruments are being evaluated for their ability to measure near-surface wind flow patterns during chemical simulant, smoke/obscurant, and other field tests.

Scintillometers are designed to utilize the optical effects caused by small scale density discontinuities in the atmosphere that are transported across the optical path by the wind. These density discontinuities cause irregularities in the refractivity field (optical turbulence) that can be observed as variations in received illumination intensity (scintillations). Crosswind scintillometer transmitter and receiver apertures define spatial filters sensitive to turbulent motions at certain segments along the optical path. This sensitivity to optical turbulence is defined in terms of weighting functions that are ideally 1.0 along the desired path segments and 0 elsewhere. The weighting functions derived from wave propagation theory for spatially filtered apertures peak near the centers of the desired path segments and taper off towards the path segment edges. In real applications, weighting functions are affected by scintillometer design factors such as the shape, size, and alignment of the filters; receiver sensitivity; and the signal analysis technique used in data reduction. Because real weighting functions can deviate from theoretical results, field testing is needed to verify weighting function performance.

2.2.2. Objective

The objective of the Weighting Function Test was to verify theoretical crosswind scintillometer weighting functions. Weighting functions can be evaluated through an analysis of crosswind measurements. Specifically, the crosswind measured along the path segment defined by a specific weighting function should agree with other measurements of the crosswind taken adjacent to the path segment. A weighting function should, at the same time, remain insensitive to the wind at other positions along the optical path. Two criteria were used to verify weighting functions: (1) a high degree of correlation between crosswind measurements obtained along adjacent segments using two parallel scintillometer paths coupled with low correlation between non-adjacent path segment measurements, and (2) a high degree of correspondence between scintillometer crosswind measurements for each path segment and measurements by a reference instrument stationed along the path segment. A similar experimental technique was used by Ochs et al. (1988) to determine the scintillometer calibration constant. Qualitative evaluations of time series data rather than correlation coefficients were used for the second criterion because of inherent differences between path-averaged scintillometer measurements and measurements obtained from fixed positions along the optical path.

2.2.3. Instrumentation

Instrumentation used in the weighting function test included a crosswind scintillometer transmitter and two receivers, five sonic anemometers, and several data loggers. Two scintillometer receivers placed adjacent to each other were used with a single transmitter to establish two quasi-parallel optical paths. The sonic anemometers were stationed at the centers of the optical path segments. The analog data were recorded on the data loggers.

Crosswind scintillometer operation is based on a spatially filtered aperture technique proposed by Lee (1974). The refractivity field can be represented by its Fourier decomposition products, one of which is the wavenumber or its inverse (frequency). As the refractivity field translates across an optical path, sinusoidal perturbations are generated that can be projected onto a downrange receiving plane. According to Lee, a spatial filter of wavelength w allows only one wavenumber at optical path position s to contribute to the variance of illumination intensity at the receiver. Therefore, transport of turbulence by the wind across path position s can be measured as a temporal frequency f across the photodiode array in the receiver output. For ideal filters and a non-rotational wind field, all variance observed at the receiver output must originate at s . With multiple source and receiver apertures creating several spatial filters of different sizes, crosswind components at several positions along the optical path can be simultaneously determined.

The crosswind profiling spatially averaged filter scintillometer Model II developed for DPG by NOAA ERL/WPL (Ochs et al., 1988) uses incoherent apertures containing several sizes of zero-mean filter elements. Combinations using the various transmitter and receiver filters produce spatial filters of wavelength w , with weighting functions designed to peak at five segments along an optical path of length L . The filter combinations are chosen such that weighting functions peak at the $1/5$, $1/3$, $1/2$, $2/3$, and $4/5$ path segments. Only the translation of optical turbulence elements of appropriate size across one of the five

optical path segments should produce signal strength fluctuations at the receiver, where the scintillation pattern image is focused onto a photo-diode array. The product of f (second^{-1}) with the spatial filter of wavelength w (meters) defines a crosswind, cw (meters per second) for each path segment

$$cw = Kfw \quad (11)$$

where K is a calibration coefficient.

Transmitter and receiver aperture design defines the w used in Equation (11) and the path positions s for the spatial filter weighting functions. The transmitter optics consist of a 0.94- μm light emitting diode (LED) radiating over a 1.8-mm diameter hemisphere as a source, with a ground glass diffuser to enlarge its radiating area to 29- by 40-cm. Two Fresnel lenses with sets of alternating clear and reflecting stripes form zero-mean filters (d_t) of 20- and 5-cm wavelengths on the transmitter. Receiver optics consist of one 29- by 40-cm Fresnel lens forming three pairs of zero mean filters (d_r) of 5-, 10-, and 20-cm wavelengths. Ratios of the transmitter and receiver zero mean filter wavelengths define spatial filters of wavelength w at path position s , as given by

$$w = d_r d_t / (d_r + d_t) \quad (12)$$

$$s = L / (1 + d_r / d_t) \quad (13)$$

The resultant spatial filter weighting functions peak at positions along the optical path as shown in Figure 2. Fractional path position s/L is defined between zero ($s/L = 0.0$) at the transmitter and one ($s/L = 1.0$) at the receiver. The relationships given by Equations (12) and (13) between zero-mean filter element size (d_r , d_t), fractional path position, and spatial wavelength are presented in Table 7.

In addition to crosswind speed, the sign of the wind crossing direction must be defined. The crosswind sign is determined by analysis of the covariance of the signals focused on the receiver's photodiode array. The Model II profiler scintillometer uses a set of shift registers to create a second signal shifted one-fourth of a wavelength from the first for this purpose. The results from combinations of summations at 14 time lags on the covariance function define the crosswind sign. The established sign convention is that air movement from left to right as viewed from the receiver looking towards the transmitter produces a positive crosswind. A detailed description of the crosswind profiler scintillometer design and operation is given by Ochs et al. (1988).

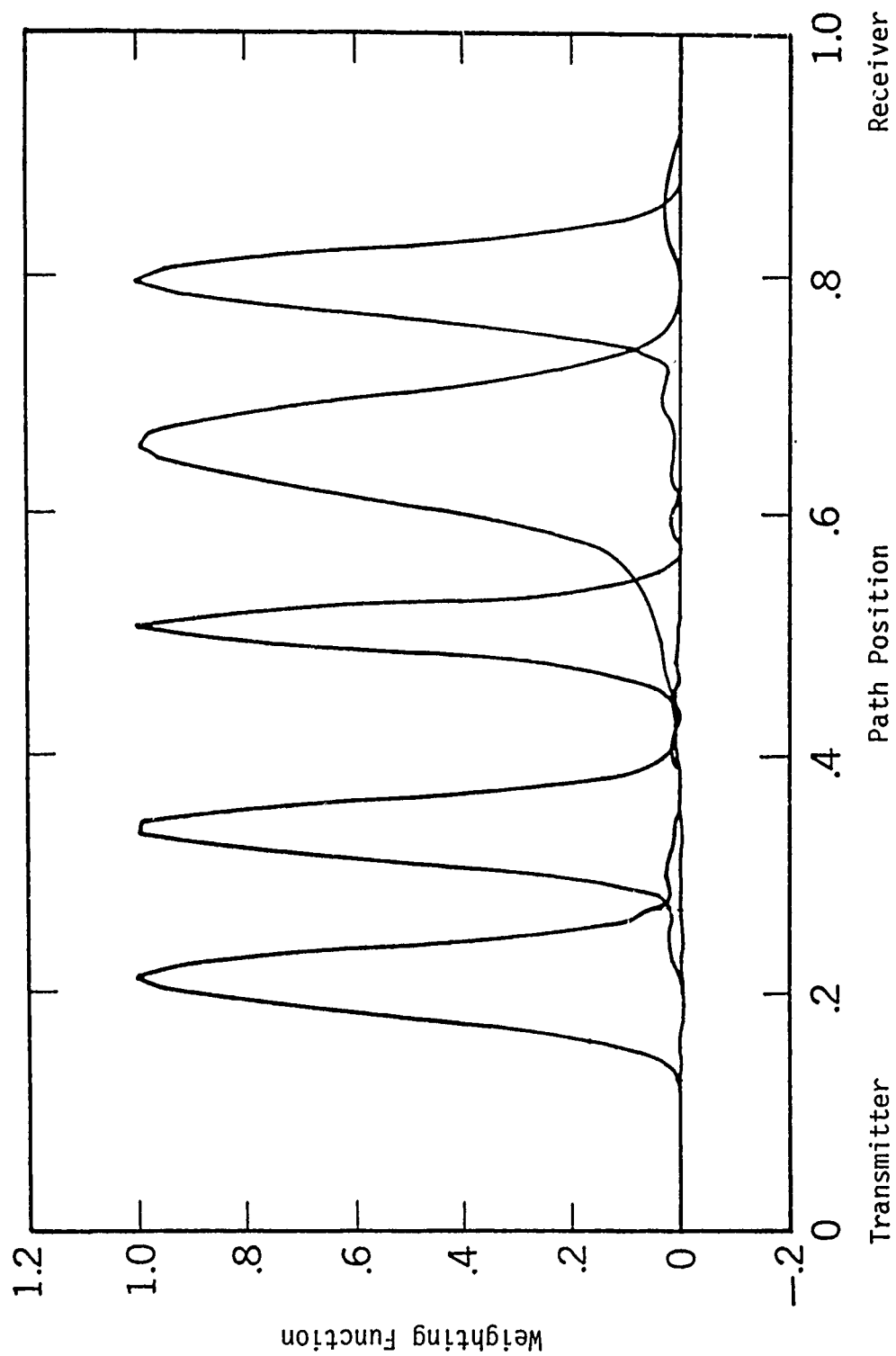


Figure 2. Calculated Path Weighting Functions with Peaks at the $1/5$, $1/3$, $1/2$, $2/3$, and $4/5$ Path Positions (Courtesy of Gerard Ochs, NOAA ERL/WPL).

Table 7. Relationship Between Transmitter/Receiver Filter Element Size, Path Position, and Spatial Wavelength.

Zero-Mean Filter		Path Position s/L	Spatial Wavelength λ (cm)
Transmitter d_t (cm)	Receiver d_r (cm)		
5	20	1/5	4.00
5	10	1/3	3.33
5	5	1/2	2.50
20	10	2/3	6.67
20	5	4/5	4.00

Five sonic anemometers were positioned along the scintillometer optical path to provide wind data for comparison with the scintillometer crosswinds. The sonic anemometers used were two RSWS-201 two-axis (#605 and #608) and three RSWS-301 three-axis (#303, #304, and #305) sonic anemometers manufactured by Applied Technologies, Inc. (ATI). These instruments consist of orthogonal sets of acoustic transmitter/receivers with a transducer separation distance d of 15 cm. The two-axis sonic anemometer arrays provide orthogonal measurements of the horizontal (u and v) wind components, while the three-axis arrays provide an additional measurement of the vertical (w) wind component. The sonic anemometer axis orientation is defined by the alignment of the u -component transmitter-receiver pair, which is parallel to the mounting boom. A positive sign is assigned to wind components moving towards the front of the array, from left to right across the array, and upwards from below the array.

The sonic anemometer's basic unit of measure is time t . Each transmitter emits an ultrasonic adiabatic compression wave that propagates towards its paired receiver at a velocity equal to the sum of the local speed of sound c plus the wind velocity component (u , v , or w). An inverse transit time solution for each velocity component is used to eliminate c from the solution. Thus, the cross-axis velocity component v is a function of d and the transit times between transducers

$$v = \frac{d}{2} \left[\frac{1}{t_1} - \frac{1}{t_2} \right] \quad (14)$$

where t_1 is the compression wave travel time from transducer 1 to transducer 2 and t_2 is the travel time in the opposite direction. The measurement velocity resolution is 0.01 m s^{-1} , while the spatial resolution is defined by the 15-cm pathlength. Consequently, the sonic anemometers provided fast-response, high resolution point measurements of wind components for comparison with the crosswind scintillometer measurements. Further information on sonic anemometers is provided by Biltoft (1987).

The Weighting Function Test data from the sonic anemometers and crosswind scintillometer receivers were recorded at 1 Hz on Campbell Scientific CA21X

Micrologger data loggers. This data rate sampled essentially all of the output from the scintillometers, but only 10 percent of the output from the sonic anemometers. The data collection shortfall, which was imposed by the limitations of the data collection system, also limited the types of data analysis that could be done. However, sufficient data were obtained for simple inter-comparisons that partially satisfied the Weighting Function Test objective. Data from both the sonic anemometers and crosswind scintillometers were averaged to 5-s intervals for intercomparison. This temporal averaging smoothed some high frequency velocity fluctuations in the sonic anemometer data and produced results that were more comparable to the spatially-averaged scintillometer data.

2.2.4. The Weighting Function Test

The Weighting Function Test was designed to verify crosswind scintillometer weighting functions by intercomparing crosswind scintillometer winds with each other and with wind measurements from sonic anemometers stationed at positions along the optical path. Figure 3 shows the test configuration. Optical paths were established between a transmitter located near Mesonet Station #1 and two adjacent receivers located in an open window on the south wall of the Tower Grid Command Post. This arrangement established two quasi-parallel optical paths with north-south orientations at a height of 2 m above flat, unobstructed ground covered by grasses and low shrubs. The sonic anemometer line was set up parallel to and 2 to 3 m to the east of the optical paths. The sonic anemometer transducers were aligned towards the south (into the wind) and were at approximately the same height as the optical paths. Therefore, air movement from the east to the west across the optical path would register as a positive crosswind for the scintillometers and as a positive v-axis component for the sonic anemometers. Figure 3 includes the locations of the five path segments defined by weighting function peaks and the sonic anemometer positions.

Scintillometer weighting functions are difficult to verify in the ambient atmosphere because wind components along the path are correlated to unknown degrees over the optical path. These correlations also continuously change in response to the atmosphere's dynamical forcing functions. Consequently, it is difficult to isolate the contribution by crosswinds at one path segment from contributions by crosswinds at other path segments. One way to override undesired correlations is to impose an artificial perturbation on the wind field that can be moved from one path segment to another. This moving perturbation effect was achieved by flying a UH-1 helicopter slowly along a path adjacent to the optical path at 20 to 30 m above ground level. As shown by Figure 4, the helicopter's rotor wash created decorrelating perturbations that were observed as rapid changes in sonic anemometer v-component measurements. The scintillometer's response to these effects serves as a basis for analysis of weighting function performance.

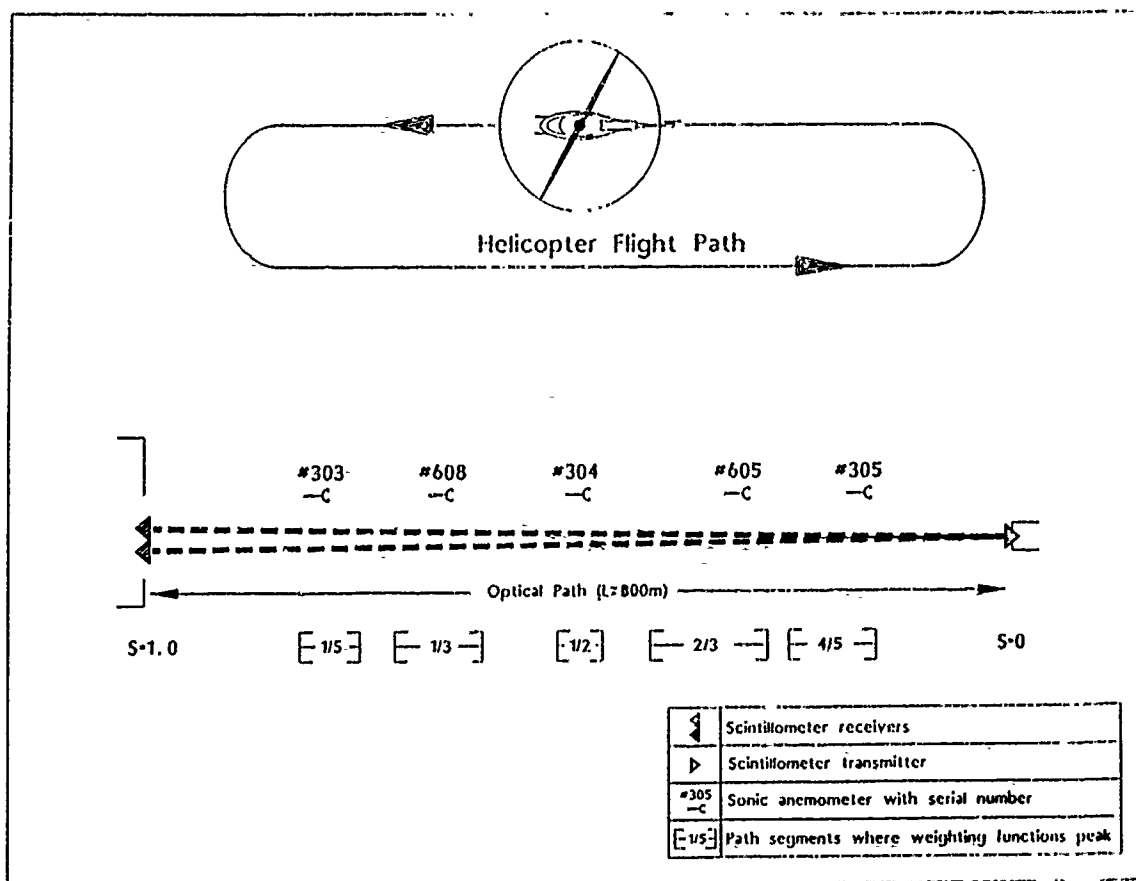


Figure 3. Weighting Function Test Configuration.

2.2.5. Weighting Function Analysis

The first Weighting Function Test criterion required intercomparison of results from the two crosswind scintillometer receivers set up with adjacent parallel paths. Simple correlations between path segment measurements were used as a measure of weighting function response. While it is not possible to derive quantitative conclusions from correlations of serial data sets (the correlation equation is derived under the assumption that the samples are independent), simple correlations are useful for illustrating the relative response of each instrument's weighting functions to wind perturbations at various positions along the optical path.

Table 8 is a matrix of correlation coefficients between the path position 5-s average crosswinds measured by scintillometer receivers #2 and #3. The three-digit figures used to bound the matrix consist of the receiver serial number (2 or 3) followed by path segment position (15 for the 1/5 path position, 13 for the 1/3 path position, etc.). With the exception of missing data for the 4/5 path position on Unit #2, correlations between the adjacent path segment crosswinds are high (0.95 or better), while non-adjacent path correlations are considerably lower. These results indicate that the scintillometer

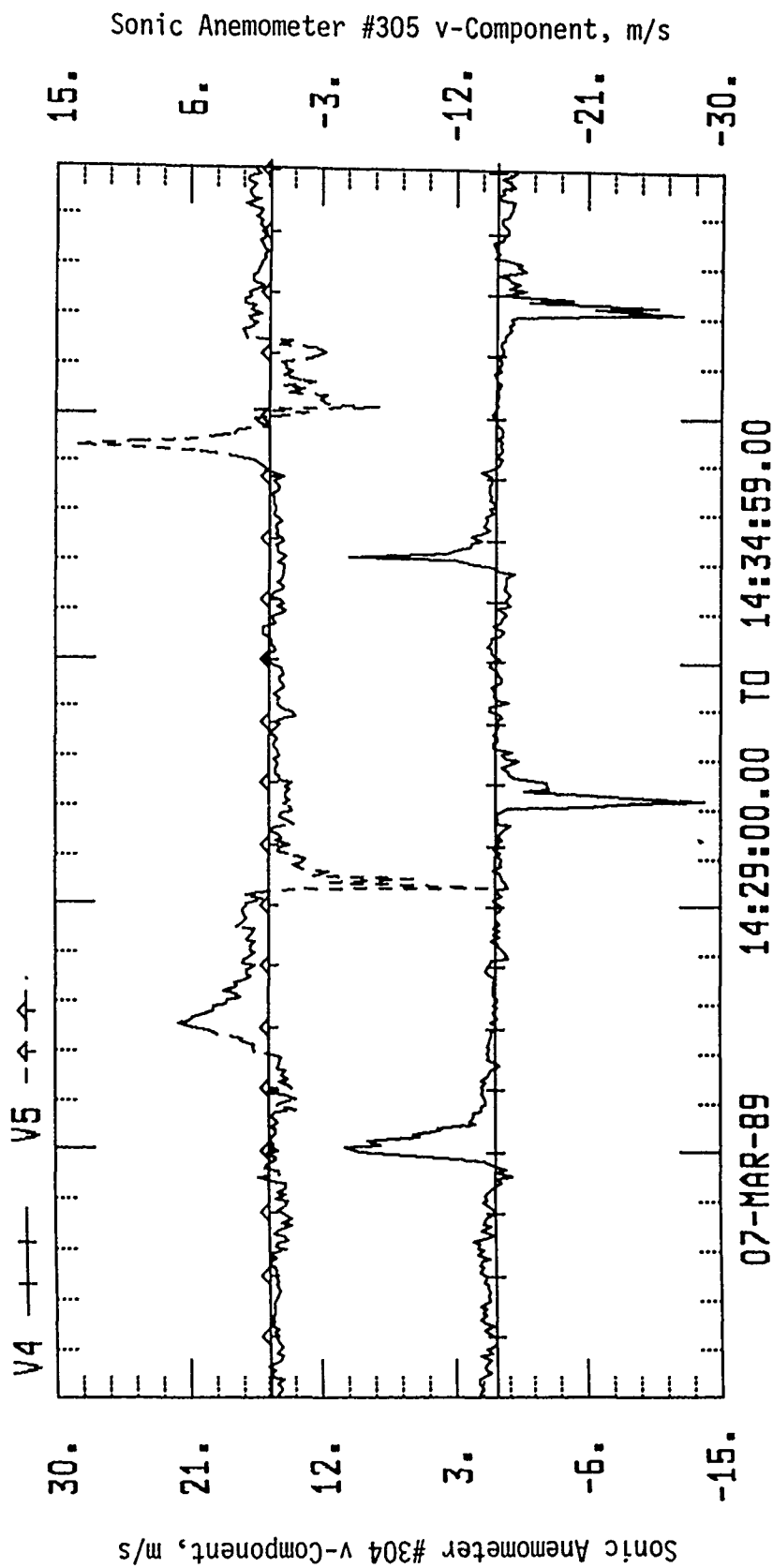


Figure 4. Sonic Anemometer 1-Hz Wind v-Component Measurements from Unit #304 Near Center of Optical Path (lower plot) and Unit #305 Near Scintillometer Transmitter (upper plot).

receivers are performing in the same fashion. The correlation coefficients in Table 8 also reveal elevated correlations (greater than 0.7) between crosswinds from the 2/3 path segments and the 1/5 and 1/3 path segments. These elevated correlations indicate that the path weighting function curves are broader than predicted by theory. Comparisons with sonic anemometer data are used below to reveal further details of these effects.

Table 8. Correlation Coefficients for 5-s Average Crosswinds Measured by Scintillometers #2 and #3.

	315	313	312	323	345
215	.95	.54	.41	.77	.18
213	.59	.97	.32	.72	.23
212	.47	.29	.98	.52	.58
223	.81	.75	.43	.98	.29
245	ND ^a	ND	ND	ND	ND

^aMissing data for Scintillometer #2 4/5 path position.

Figure 5 shows time series plots of the mid-path (1/2 path segment) scintillometer crosswinds and the mid-path sonic anemometer (#304) v-component. These plots illustrate the relative performance of the scintillometer and sonic anemometer in a wind field punctuated by periods of extreme turbulence. Note that the 5-s average wind components in the figure have been subjected to a mean removal algorithm so that the plotted points represent deviations from the mean for each data set. Figure 5 illustrates a generally good qualitative correspondence between the scintillometer and sonic anemometer crosswinds. The scintillometer trace exhibits broader peaks, but these are expected because of path averaging effects. The scintillometer trace also contains a spurious spike (indicated by the arrow in Figure 5) not seen in the sonic anemometer data. This is an example of the difficulties encountered by the scintillometer's signal analysis routine as the sign of the crosswind component abruptly changes. These changes occasionally cause the scintillometer servo to lock onto the wrong sign, producing a spurious spike in the data (see Biloft, 1988).

Direct intercomparison of scintillometer 1/3 and 2/3 path position crosswinds with sonic anemometer data was not possible because sonic anemometer #605 was blown down by rotor wash, and the data logging system failed for anemometer #608. However, the times of passage of rotor wash through the 1/3 and 2/3 path segments could be estimated using the times of passage over the anemometer #303, 304, and 305 positions. The estimated times of passage at the 2/3 position are indicated by arrows in Figure 6 above the 5-s average crosswinds from the 2/3 path positions of scintillometer units #2 and #3. Visual inspection of Figure 6 strongly suggests that the 2/3 path segment weighting functions are responding to more than just the passage of rotor wash through the 2/3 path segment. Comparison with the times of passage through other path segments

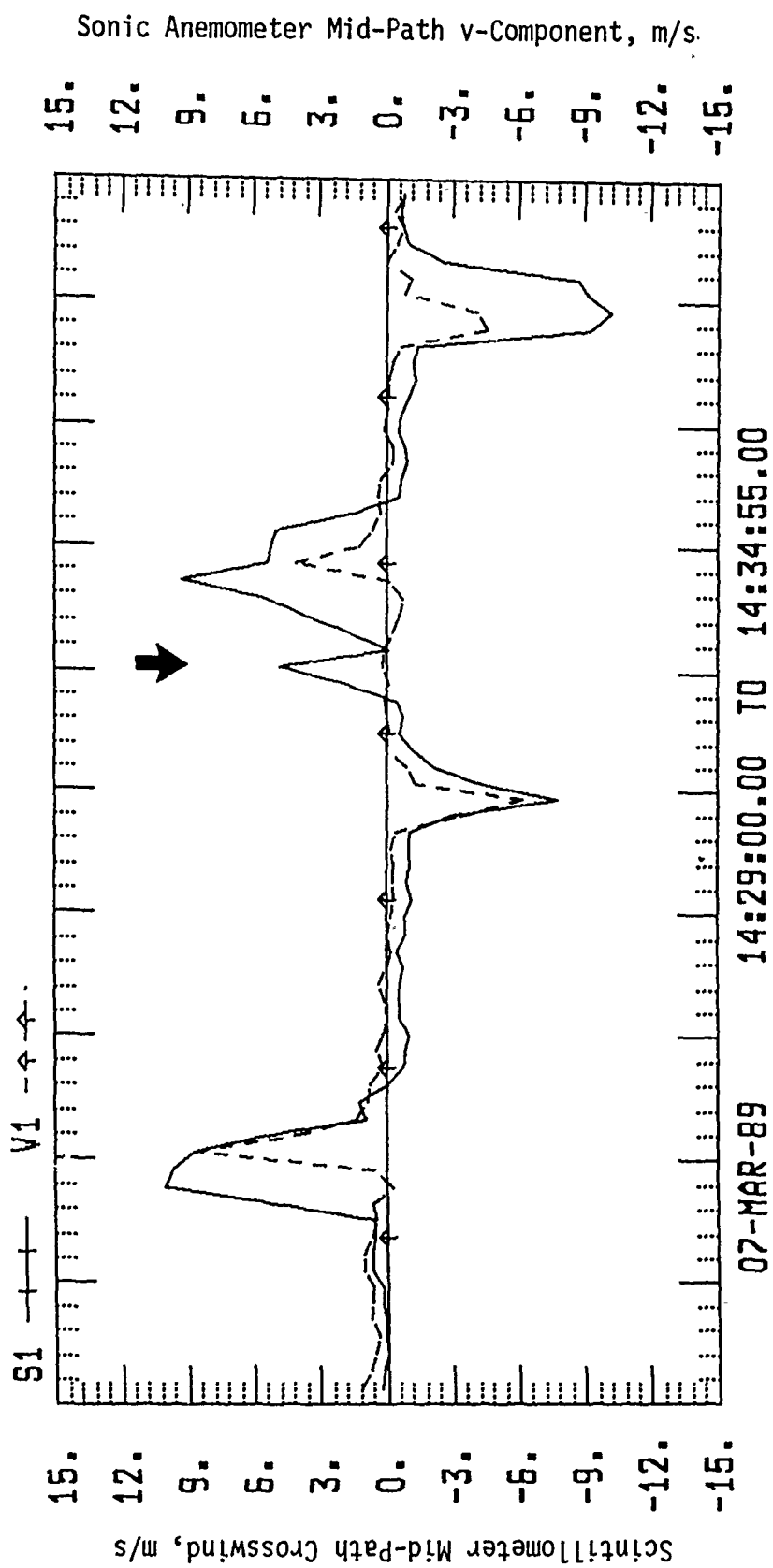


Figure 5. Time Series Plot of 5-s Averaged 1/2 Path Segment Crosswinds from Scintillometer #3 (solid line) and v-Component Wind (dashed line) from Sonic Anemometer #304. The Spurious Peak in the Crosswinds is Indicated by an Arrow. Both Data Sets Were Subjected To Mean Removal.

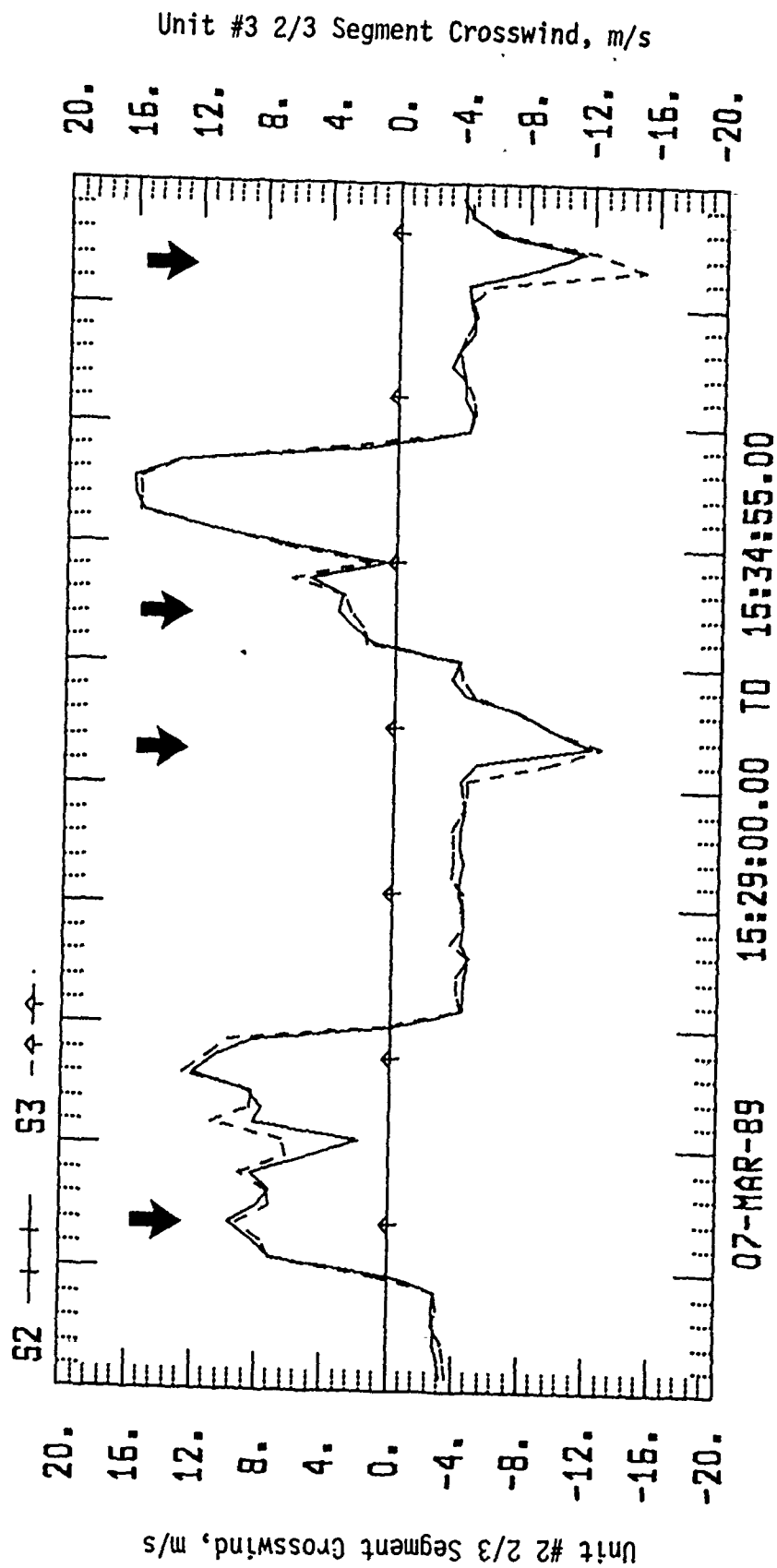


Figure 6. Crosswinds from the 2/3 Path Position for Scintillometers #2 (solid line) and #3 (dashed line). Arrows Indicate Estimated Rotor Wash Passages Through the 2/3 Path Position. Both Data Sets were Subject to Mean Removal.

indicates that the additional peaks on Figure 6 correspond to rotor wash in vicinity of the 1/3 and 1/5 path positions. This is likely to be the cause of the elevated correlations shown for these positions in Table 8. A similar effect was also observed to a lesser extent with the 1/3 path position data. Traces for the 1/5 and 4/5 path segments were more like the one shown in Figure 5 for the 1/2 path position, indicating that the weighting functions for these path segments do not exhibit excessive response to crosswinds elsewhere along the path.

2.2.6. Results

The objective of the crosswind scintillometer weighting function test was partly achieved. Weighting function performance for scintillometer receiver units #2 and #3 were highly correlated, indicating that the weighting functions are virtually identical for the two receivers. The correlation matrix used to evaluate path segment weighting function performance indicated unusually high correlations between the 2/3 path segment and the 1/3 and 1/5 path segment crosswinds. More detailed examination of the 2/3 path segment crosswinds yielded evidence that the 2/3 path weighting function is broader than predicted by theory, exhibiting sensitivity to crosswinds near the 1/3 and 1/5 path segments. However, weighting functions for the 1/2, 1/5, and 4/5 path segments exhibited little sensitivity to crosswinds outside their designated path segments. These weighting functions are therefore considered to be near their theoretical values. The weighting function for the 1/3 path segment performed considerably better than that of the 2/3 path segment, but did exhibit noticeable sensitivity outside its designed path segment. Data logging limitations and instrumentation failures prevented the collection of sufficient data for a more thorough analysis using spectrum analysis techniques.

2.2.7. Conclusions

The prototype crosswind profiler scintillometer comes very close to satisfying the need for a remote crosswind measurement capability. However, it appears that some adjustments are required to correct weighting function response for the 2/3 and 1/3 path segments and to eliminate errors generated as the sign of the crosswind changes. With these limitations in mind, scintillometers can be used to generate valuable data for test support.

The use of helicopter rotor wash to generate wind field perturbations constituted a severe test for both the scintillometers and sonic anemometers. The scintillometer cannot respond as well as the sonic anemometer to the rapid velocity fluctuations and changes in crossing wind direction generated by rotor wash. This should not be considered a serious limitation for test support applications because the atmosphere seldom generates such highly turbulent wind conditions. Further weighting function tests should be conducted under less turbulent conditions.

2.2.8. Recommendations

Further weighting function development and testing are needed to advance the prototype crosswind scintillometer to operational status. DPG is currently the Army project manager for an SBIR project with Scientific Technologies, Inc. that is making progress towards this goal. This development effort should continue to receive support from the Army test and evaluation community.

2.3 RADIATION EFFECTS ON A THERMOMETER PROBE

2.3.1. Background

The design of a thermometer with an accuracy of 0.01 °C for micrometeorological applications requires more than just careful attention to the details of thermometer design. A major source of ambient air temperature measurement inaccuracy is the sensor's absorption of heat from sources other than the air, solar radiation being a major contributor. Unshielded sensors provide temperature readings with a positive bias during the day and a negative bias at night (Fuchs and Tanner, 1965). This effect is most pronounced in light wind conditions. Shields are frequently used in micrometeorological applications to minimize radiation effects. Unfortunately, shields restrict air flow around the sensor and bias the sensor's measurement with the temperature of the shield. This can be partly compensated by aspirating the shield, but even with the best of the aspirated shields some bias will be present as long as the shield temperature differs from the air temperature. An accurate micrometeorological thermometer therefore requires a sensor design that minimizes temperature bias, the difference between sensor temperature (T) and air temperature (T_∞). This note uses a heat balance model developed by Luers (1990) to examine possible sources of temperature bias for the TACAN quartz crystal fiberoptic temperature sensor and evaluates several methods for minimizing the instrument's measurement bias.

2.3.2. Heat Transfer Relationships

The performance of a temperature measurement system depends upon the exchange of energy between the sensor and its surroundings. The TACAN thermometer quartz probe is assumed to remain in thermal equilibrium with the metallic can that serves as its protective housing. This is justified by the close contact between the housing and the sensor, and by the housing's dominant contribution to the thermal mass of the probe assembly. With this assumption in place, heat transfer between the housing (a cylinder of radius r and length L) and its surroundings becomes the central issue.

Sensor heat balance in millicalories per second is defined in terms of the time rate of temperature change ($\partial T / \partial t$) for a sensor of mass m and specific heat C . Following Luers (1990),

$$mC\partial T / \partial t = q_{\text{abs}} - q_{\text{emit}} - q_{\text{conv}} + q_{\text{elec}} + q_{\text{cond}} \quad (15)$$

where q_{abs} and q_{emit} are absorbed and emitted radiation, q_{conv} is convective heat exchange between the sensor and the environment, and q_{cond} and q_{elec} depict sensible heat conduction and electrical heating effects through lead wires connecting the probe to its oscillator. The focus of this discussion is on the relative magnitudes of heat absorbed and emitted through the radiative terms and transferred through the convection term. Contributions from the other terms in Equation (15) will be included after they are defined.

Absorbed radiation is dependent upon the exposed surface area A , wavelength-dependent absorptivity α , and radiation intensity I . Radiation effects

can be defined in integral form as a function of wavelength λ and solar elevation as

$$q_{\text{abs}} = A(\theta) \int_{\lambda} \alpha(\theta, \lambda) I(\theta, \lambda) d\lambda \quad (16)$$

where θ , the elevation of the sun above the horizon, is virtually the same as the angle of the sun to a ground-based vertically mounted sensor. Radiative effects, for the purpose of this estimation technique, are assumed to be independent of the sun's azimuth angle.

The variables α and I are, for practical applications, divided into a short-wave solar band (0.28 to 3.9 μm) and a long-wave thermal band (4 to 100 μm). For a 300 K blackbody, 98 percent of its radiant energy lies between 4.8 and 70 μm . Division of heat loading effects into these solar and thermal bands is convenient because precision spectral pyranometers are sensitive at the 0.285- to 2.8- μm wavelengths, which cover most of the solar band, and precision infrared radiometers (pyrgeometers) are most sensitive between 5 and 50 μm . Readings from these two types of actinometers can therefore be considered representative of the integrated solar and thermal integrated radiation intensities in their respective bands.

The sensor radiative emissions term is defined by exposed surface area A_t , sensor temperature T , emissivity ϵ , and index of refraction η as

$$q_{\text{emit}} = A_t \sigma T^4 \epsilon \eta \quad (17)$$

where σT^4 , the blackbody radiant heat flux density, is from the Stefan-Boltzmann law for radiant emittance. The factor σ has a value of $8.26 \times 10^{-11} \text{ cal cm}^{-2} \text{ min}^{-1} \text{ deg}^{-4}$ (Kondratyev, 1969). Emissivity is the ratio of the radiant intensity of the housing surface to that of a black body at the same temperature. The index of refraction for air is essentially 1.0 for the purposes of emissions computations.

The q_{conv} term in Equation (15) describes the convective transfer of energy between the air and the sensor. Following Luers (1990), the magnitude of this term is determined by sensor surface area, a heat transfer coefficient h_c , and the temperature difference between the sensor and ambient air $T - T_{\infty}$.

$$q_{\text{conv}} = A_t h_c (T - T_{\infty}) \quad (18)$$

where h_c is a function of the Nusselt number, which is a function of the Reynolds number (Fand and Keswani, 1972). The effect of wind speed on the sensor temperature enters Equation (18) through the Reynolds number.

2.3.3. Sensor Exposed Area

The quartz crystal sensor housing of radius r and length L is assumed to be mounted in the upright position. Parallel rays of incoming solar radiation will impinge on varying portions of the cylinder surface, depending on the

sun's elevation angle. Diffuse radiation is assumed to be uniformly distributed. Sensor housing conductivity is sufficiently high that it has a uniform radiant temperature over its exposed surface area.

The total area of the cylinder includes the surface area of the side plus that of the top and bottom. However, because the cylinder bottom is effectively shielded from radiation, the exposed area A_t includes only the side and the top, or

$$A_t = 2\pi rL + \pi r^2 . \quad (19)$$

The equivalent area exposed to direct normal solar radiation A_e is a portion of the cylinder that includes the cylinder side plus the top, modified by the elevation angle of the sun, or

$$A_e = 2rL\cos\theta + \pi r^2\sin\theta . \quad (20)$$

The sun angle θ_{\max} for maximum surface area exposure to direct solar radiation I_s is found by differentiating Equation (20) with respect to θ . When this derivative is set to zero, the result is

$$\tan\theta_{\max} = \pi r/2L . \quad (21)$$

Equation (21) provides θ_{\max} for a given r/L ratio. To minimize solar radiation effects, the ratio of r to L should be small. For small r/L ratios ($r/L < 0.2$), Equation (21) can be approximated by

$$\theta_{\max} = 89r/L . \quad (22)$$

Thus, the maximum sensor area is exposed to solar radiation at low sun elevation angles where the solar radiation I_s is relatively weak.

2.3.4. Radiative Properties of Surfaces

Heat transfer between the sensor housing and its environment is strongly influenced by the radiative properties of the housing. The radiative properties governing heat transfer for an ideal opaque surface are the absorptivity α , emissivity ϵ , and reflectivity ρ . Kirchhoff's law for blackbodies equates α and ϵ , and these properties are related to ρ by

$$\alpha = \epsilon = 1 - \rho . \quad (23)$$

Equation (23) is strictly applicable only to clean, homogeneous, opaque, optically smooth surfaces. As discussed below, the "ivities" represented in idealized radiative transfer equations are approximated by the "ances", the

measured properties of real surfaces. Following Touloukian et al. (1972), these properties are defined as follows:

Emittance ($\epsilon_{\phi, \lambda}$) -- The ratio of radiant exitance (flux per unit area leaving a surface) of a body at a given temperature to that of a blackbody radiator at the same temperature.

Absorptance ($\alpha_{\phi, \lambda}$) -- The ratio of absorbed flux to incident flux.

Reflectance ($\rho_{\phi, \lambda}$) -- The ratio of reflected flux to incident flux.

The "ances" are highly dependent upon the characteristics of the surface, wavelength of the radiation, and angle ϕ between the incident radiation and the normal to the surface. Touloukian et al. (1972) use subscript ϕ to denote directionality ($\phi=0$ for normal incidence, $\phi=2\pi$ for hemispherical) and subscripts s and t to denote solar and thermal spectral bands. Reflectance is the most easily measured property of surfaces and is therefore the most widely reported property. Touloukian et al. (1972) frequently derive absorptance from room temperature reflectance data using Equation (23), while emittance is independently determined.

Touloukian et al. (1972) use a ratio of normal solar absorptance $\alpha_{(0,s)}$ to the hemispherical total emittance $\epsilon_{(2\pi,t)}$ to describe the radiative properties of surfaces. Polished silver surfaces, which have low α and ϵ for wavelengths greater than $3 \mu\text{m}$, come close to being total reflectors. Other metallic surfaces have the undesirable characteristic of a higher α in the solar than in the thermal bands. A high $\alpha_{(0,s)}/\epsilon_{(2\pi,t)}$ ratio is characteristic of solar absorbers and thermal reflectors. For this reason, Fuchs and Tanner (1965) recommend that metal surfaces not be used for solar radiation shields. An ideal thermometer surface should have a small ratio of normal solar absorptance to total hemispherical emittance

$$\alpha_{(0,s)}/\epsilon_{(2\pi,t)} \ll 1.0 \quad (24)$$

Some white paints approach this ideal condition. Grum and Luckey (1968) report a spectral reflectance in the solar range of 0.98 for barium sulfate. However, paints degrade with exposure to ultraviolet radiation unless treated with some additional coating. An optical solar reflector (OSR) surface, as reported by Greenberg et al. (1967), provides the closest approach to an ideal thermometer surface. Touloukian et al. (1972) report a solar absorptance of 0.047 and a hemispherical total emittance of 0.74 for a typical OSR surface. For illustrative purposes, α is assumed to be 0.2 in the solar and 0.05 in the thermal bands, with equivalent ϵ . These values are typical of the polished metal housings found on the quartz crystal thermometers.

2.3.5. Calculation of Radiation Intensities

Radiation intensity, which is defined in terms of heat gain per unit time on a unit area, includes effects from both direct and diffuse solar and thermal radiation components. All radiation components will vary with atmospheric moisture content, turbidity, optical airmass, and cloud cover. Clear sky conditions were chosen for heat balance computations because these conditions

offer maximum exposure to direct solar radiation and are most likely to maximize temperature bias.

A combination of measured and estimated radiation intensities was used in this heat balance study. Palmer and Hansen (1956) used a pyroheliometer to measure direct beam solar radiation I_s at DPG. A sample of their July maximum hourly I_s in millicalories per square centimeter per second is presented in Table 8 along with intensities impinging on horizontal (I_h) and vertical (I_v) surfaces, which are calculated as the products of I_s with the sine and cosine of the sun's elevation angle. No satisfactory method is available for calculating diffuse solar radiation I_d from I_s , but a review of clear sky radiation data collected at Davis, California (Morgan et al., 1970) indicates that I_d is approximately 15 percent of I_s under clear conditions for most θ . This percentage was used to obtain the Dugway I_d data presented in Table 8. Thermal diffuse radiation I_t was also estimated using the Morgan et al (1970) results. The simple empirical relationship between counter radiation in calories per square centimeter per minute and ambient temperature in degrees Celsius at Davis, California of

$$I_t = 0.35 + 0.005T_{\infty} \quad (25)$$

was used to estimate clear sky thermal diffuse radiation. The results from Equation (25), converted to millicalories per square centimeter per second, are also presented in Table 9.

Table 9. Measured Clear Day Maximum Direct Solar Radiation Intensities and Estimates of Diffuse Solar and Thermal Radiation Intensities as a Function Of Time Of Day At Dugway, Utah.

Time (MST)	Sun Angle (Deg)	Radiation Intensity ($\text{mcal cm}^{-2} \text{s}^{-1}$)				
		Solar Direct	Solar Horizontal	Solar Vertical	Solar Diffuse	Thermal Diffuse
06	07	2.00	0.17	2.00	0.33	7.52
07	18	6.33	2.00	6.00	1.00	7.93
08	29	11.17	5.33	9.83	1.67	8.54
09	41	16.50	10.83	12.50	2.50	8.91
10	52	20.00	15.83	12.33	3.00	9.24
11	62	23.00	20.33	10.83	3.50	9.27
12	70	24.50	23.00	8.33	3.67	9.37
13	71	25.50	24.17	8.33	3.83	9.38
14	65	24.17	21.83	10.17	3.67	9.42

2.3.6. Calculation of Absorbed Radiation

The radiation absorbed by the sensor housing is given by the sum of the contributions from direct and diffuse radiation components. Absorbed direct

radiation is the product of the horizontal and vertical exposed areas with the corresponding radiation intensities and the absorptance

$$q_{\text{abs}}(\text{direct}) = (2rL)I_v \alpha_{(0,s)} + (\pi r^2)I_h \alpha_{(0,s)} \quad (26)$$

Absorbed diffuse solar radiation is the product of the exposed cylinder area A_t , solar absorptance (hemispherical), and the diffuse solar intensity

$$q_{\text{abs}}(\text{diffuse solar}) = (2\pi rL + \pi r^2) \alpha_{(2\pi,s)} I_i \quad (27)$$

Similarly, absorbed diffuse thermal radiation is a product of A_t , the hemispherical thermal absorptance, and the diffuse thermal intensity

$$q_{\text{abs}}(\text{diffuse thermal}) = (2\pi rL + \pi r^2) \alpha_{(2\pi,t)} I_t \quad (28)$$

The calculated direct, diffuse solar, diffuse thermal, and total absorbed radiation in millicalories per second for a sensor housing of 1-mm radius and 1-cm length are shown in Table 10.

Table 10. Calculated Direct, Solar Diffuse, and Thermal Absorbed Radiation for a Metallic Cylindrical Housing of 1 mm Radius and 1 cm Length Exposed to Maximum Solar Radiation Intensities At DPG.

Time (MST)	Sun Angle (degrees)	Absorbed Radiation (mcal s ⁻¹)			
		Solar Direct	Solar Indirect	Thermal Diffuse	Total
06	07	0.08	0.04	0.25	0.37
07	18	0.25	0.13	0.26	0.64
08	29	0.43	0.22	0.28	0.93
09	41	0.57	0.33	0.29	1.19
10	52	0.59	0.40	0.30	1.29
11	62	0.56	0.46	0.31	1.33
12	70	0.48	0.48	0.31	1.27
13	71	0.49	0.50	0.31	1.30
14	65	0.54	0.48	0.31	1.33

2.3.7. Calculation of Emitted and Convective Radiation

The use of Equations (17) and (18) to calculate emitted and convective radiation requires knowledge of the temperature of the sensor housing and the ambient air temperature. If $\partial T/\partial t$ in Equation (15) is assumed to be negligibly small and the conductivity and electrical heating terms are neglected,

$$q_{\text{abs}} = q_{\text{emit}} + q_{\text{conv}} \quad (29)$$

By selecting a representative air temperature T_{∞} , the sensor temperature T can be determined, and with it the magnitudes of q_{emit} and q_{conv} .

The heat transfer coefficient of Equation (18) is given by

$$h_c = \text{Nu}/d \quad (30)$$

where Nu is the Nusselt number, k is thermal conductivity of air (6.30×10^{-5} cal $\text{cm}^{-1} \text{s}^{-1} \text{°C}^{-1}$ at 30 °C), and d is the probe diameter. The Nusselt number is a dimensionless thermal flux computed as a universal function of the Reynolds number Re . Fand and Keswani (1972) suggest that heat transfer from cylinders to air in cross flow over a range of $10^{-2} < \text{Re} < 2 \times 10^5$ can be described by

$$\text{Nu} = 0.184 + 0.324\text{Re}^{0.5} + 0.291\text{Re}^m \quad (31)$$

where

$$m = 0.247 + 0.0407\text{Re}^{-0.168} \quad (32)$$

For a representative wind velocity U of 2 m s^{-1} and a 0.2-cm diameter housing, Re is 246. This produces a Nusselt number of 6.51 and an h_c of $2.05 \text{ mcal cm}^{-2} \text{s}^{-1} \text{°C}^{-1}$. Solutions for $(T-T_{\infty})$, q_{emit} , and q_{conv} , with total q_{abs} taken from Table 10, are given in Table 11 for representative values of air temperature measured on a warm July day (20 July 1989) at DPG.

Table 11. Calculated Emitted and Convective Radiation Transfer Rates for Representative July Temperatures At Dugway, and Emissivity of 0.05.

Time (MST)	Sun Angle (deg)	Temperatures (°C)		q_{abs} (mcal s^{-1})	q_{emit} (mcal s^{-1})	q_{conv} (mcal s^{-1})
		T_{∞}	$T-T_{\infty}$			
06	07	18.2	0.031	0.37	0.33	0.04
07	18	23.2	0.212	0.64	0.35	0.28
08	29	30.4	0.402	0.93	0.37	0.55
09	41	34.9	0.575	1.19	0.41	0.78
10	52	38.8	0.629	1.29	0.43	0.85
11	62	39.2	0.661	1.33	0.44	0.90
12	70	40.4	0.607	1.27	0.44	0.82
13	71	40.6	0.631	1.30	0.44	0.85
14	65	41.0	0.655	1.33	0.45	0.88

2.3.8. Results

The procedure described in the previous section was repeated several times to determine the effects of other heat balance equation variables on temperature bias. Wind speed, ambient temperature, and sensor size enter the heat balance equations through the convective term. Increasing U or d causes a linear increase in Re , and Nu increases approximately with the square root of Re . However, h_c contains d in the denominator, so the net result is that the heat transfer coefficient increases approximately with the square root of velocity and decreases with the square root of sensor diameter. As shown by Figure 7, the effects of U on $(T-T_\infty)$ follow an exponential relationship with a dramatic increase in temperature bias for wind speeds of less than 2 m s^{-1} . This increase in $(T-T_\infty)$ at low wind speeds increases the relative magnitude of the convective term in the heat balance equation. Wind speed effects on sensor radiation balance for a sun angle of 65° and ambient temperature of 41°C are illustrated in Table 12.

Table 12. Calculated Absorbed, Emitted, and Convective Radiation Transfer Rates as a Function of Wind Speed for a Sun Angle of 65° and Ambient Temperature of 41°C .

Wind Speed (m/s)	Sensor Temperature (K)	Bias $T-T_\infty$ (K)	q_{abs} (mcal s^{-1})	q_{emit} (mcal s^{-1})	q_{conv} (mcal s^{-1})
0.16	316.059	1.859	1.334	0.880	0.453
1.00	315.080	0.880	1.334	0.882	0.451
2.00	314.855	0.655	1.334	0.886	0.447
5.00	314.637	0.437	1.334	0.889	0.445
10.00	314.519	0.319	1.334	0.890	0.444

Also shown in Figure 7 is a nearly linear curve illustrating the effects of changes in T_∞ on temperature bias. These results were obtained for a sun angle of 65° with the sensor diameter held constant at 0.2 cm and a wind speed of 2 m s^{-1} . The temperature curve in Figure 7 shows a decrease in temperature bias of -0.0013°C per degree of ambient temperature increase. This decrease in bias with temperature is accompanied by an increase in absorption and emission and decrease in heat loss due to convection, as illustrated in Table 13. Thus, heat balance equation results indicate that temperature biases of several tenths of a degree are likely to occur for a sensor of reasonably achievable size exposed to realistic ambient conditions.

Temperature Bias as a Function of Wind Speed and Ambient Temperature for 0.2 cm Diameter Probe

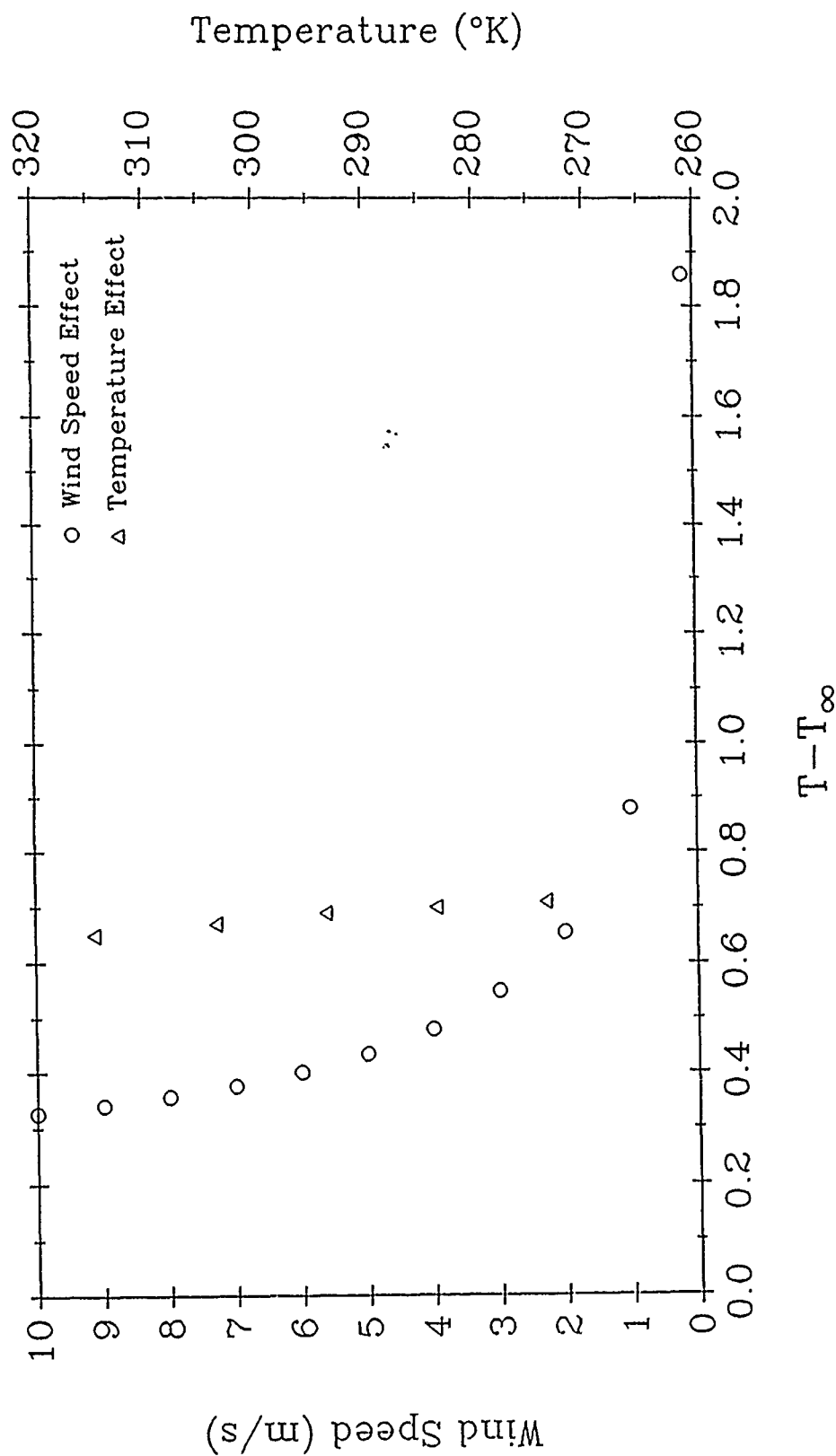


Figure 7. Temperature Bias as a Function of Wind Speed and Ambient Temperature for a 0.2-cm Diameter Sensor.

Table 13. Calculated Absorbed, Emitted, and Convective Radiation Transfer Rates as a Function of Temperature for a Sun Angle of 65 deg and Wind Speed of 2 m s⁻¹.

Ambient (°C)	Temperature Sensor (K)	Bias T-T _∞ (K)	q _{abs} (mcal s ⁻¹)	q _{emit} (mcal s ⁻¹)	q _{conv} (mcal s ⁻¹)
41	314.677	0.65	1.33	0.45	0.88
30	303.655	0.67	1.30	0.39	0.91
20	293.670	0.69	1.27	0.34	0.93
10	283.682	0.70	1.24	0.29	0.95
0	273.690	0.71	1.21	0.26	0.96

2.3.9. The Aspirated Shield Alternative

An alternative to direct wind and radiation exposure is to enclose temperature sensors in aspirated shields. By subjecting sensors to the same aspiration rate (usually 3 to 5 m s⁻¹), inter-sensor temperature biases due to variable wind velocity exposures are virtually eliminated. However, the temperature biases due to ambient solar radiation are translated into thermal effects through the shield.

For a shielded sensor, ambient radiative effects are replaced by radiative emissions of the shield, and q_{abs} becomes

$$q_{abs} = \sigma T_d^4 \epsilon_d \quad (33)$$

where T_d is the temperature of the shield duct and ε_d is its emittance. The radiative balance equation then becomes

$$\sigma T_d^4 \epsilon_d = \sigma T^4 \epsilon + h_c (T - T_\infty) \quad (34)$$

A probe of 0.2-cm diameter enclosed in a shield aspirating at a rate of 5 m s⁻¹ will have an h_c of 3.0807 mcal cm⁻² s⁻¹ °C⁻¹. The thermal emittance of the shield interior is assumed to be identical to ε for the sensor (0.05). Solutions to Equation (34) using representative values of T_∞ provide (T-T_∞) of nearly 0.25 °C for each degree of shield temperature excess over sensor temperature. To achieve a (T-T_∞) of 0.01 °C, the shield would have to be within 0.04 °C of sensor temperature, which is unlikely even for the best radiation shields. The use of radiation shields would impede the achievement of 0.01 °C absolute measurement accuracy, although highly accurate temperature differential measurements could be made using carefully shielded sensors.

2.3.10. Conclusions

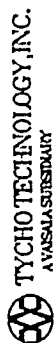
Solar radiation absorption by temperature sensors can be minimized through the use of small sensor housings made of materials designed to reflect solar and absorb thermal radiation. However, even with the smallest practical temperature housing, biases of several tenths of a degree are likely. Wind speed and ambient temperature affect the bias of sensors exposed to the open air. Aspirated shields eliminate the wind velocity component of the bias, but add a shield temperature bias. Another undesirable aspect to mechanical aspiration is that the fluctuating ambient temperature component needed for heat flux computation is lost. Sensors housed in mechanically aspirated shields produce data that are most useful for temperature differential computations.

The desired temperature measurement accuracy for micrometeorological applications is 0.01 °C. The term accuracy includes the precision, or random measurement error inherent in the instrument, plus a bias that is strongly dependent upon radiation and convection effects. It is apparent that both mechanical aspiration and direct sensor exposure can produce biases that greatly exceed the desired accuracy limits. However, it is possible to compensate through software for radiation bias by using the Luers (1990) heat balance model. Micrometeorological tower measurements often include the radiation and wind speed profile measurements that are needed for software removal of temperature bias. Bias removal through modeling radiative heat balance on unshielded sensors should be explored as a possible solution to the temperature measurement bias problem. This modeling approach will require that sensor absorptance and emittance be precisely known, which requires the use of a coating on the sensor housing that has well defined thermal and radiative characteristics and does not degrade with exposure.

2.4 RADAR WIND PROFILER PERFORMANCE OPTIMIZATION

2.4.1. Introduction

A 5-beam 404.37-MHz (74-cm wavelength) radar wind profiler was installed at DPG in May 1990. The profiler, which was designed by Tycho Technologies, Inc., provides wind speed and direction information at 250-m intervals from 500 m to 10 km and at 1000-m intervals from 8 to 16 km above ground level. Wind profiles are updated every 6 to 10 min, and these profiles are averaged to obtain hourly "consensus" averages as shown in Figure 8. The profiler's primary function is to support DPG's test mission. Located 16 km west of the Ditto Technical Center between major artillery ranges, the profiler is ideally situated to provide wind and wind shear measurements for DPG's artillery test program. Unlike pibal and radiosonde wind measurement systems, the profiler is designed for continuous unattended operation and requires no expendable flight equipment. It should provide wind information more quickly, in greater detail, and at a substantially lower cost than manual wind measurement systems.



Source: DPG
 Site: TYC101
 From: 900801 01:03 GMT
 To: 900801 12:03 GMT
 40.20 N 113.18 W
 Elev: 1293 m above MSL
 Data type: Consensus Avg.
 Param Set: Low Mode
 Shown: All Qualities
 Winds: Vertical Used
 Period: 1 hr
 Oper. Freq: 404.37 MHz

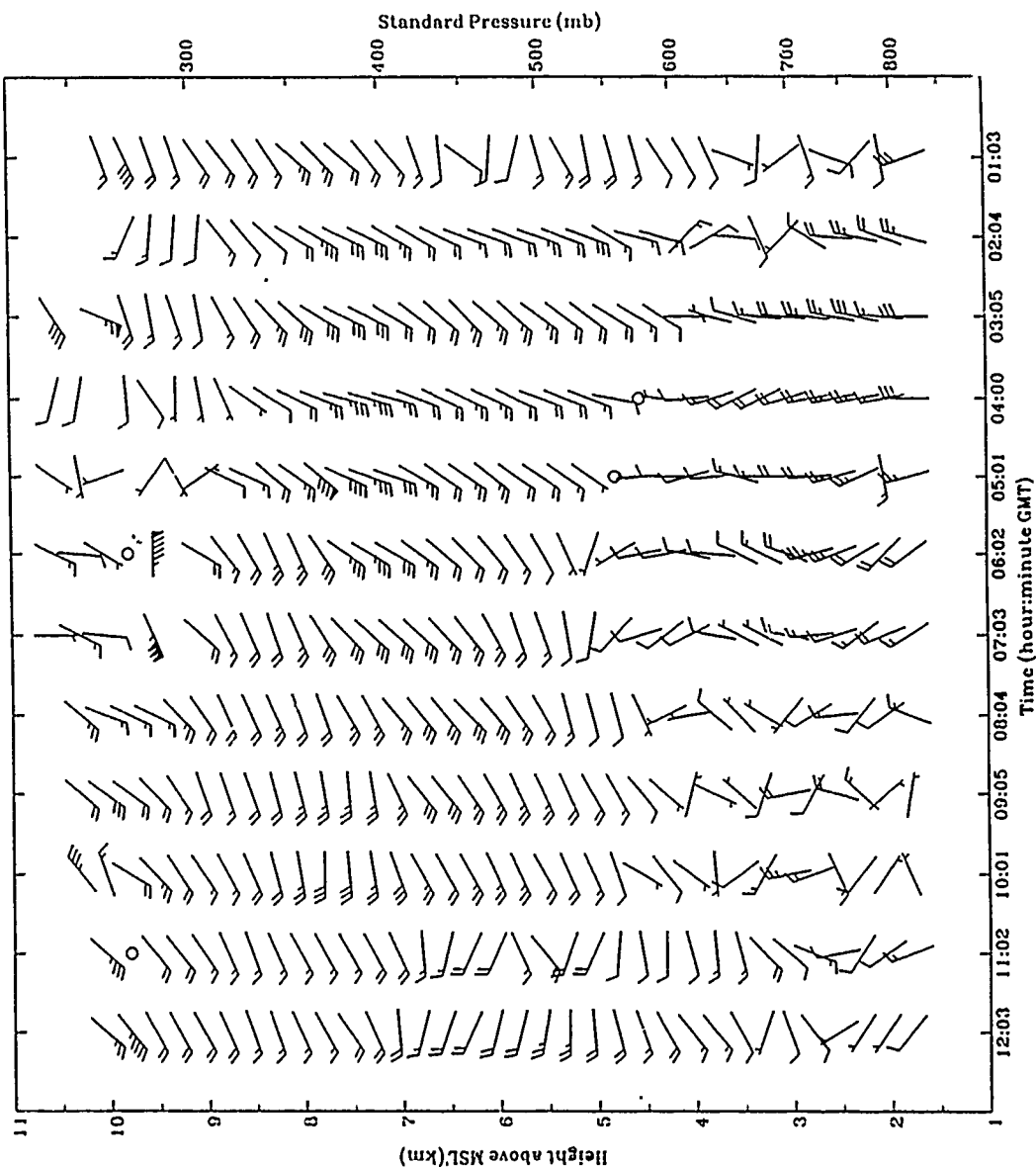
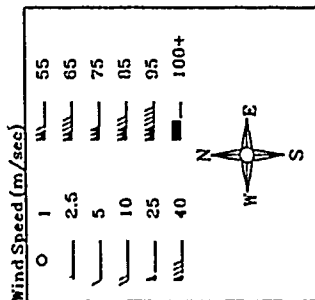


Figure 8. Hourly Consensus Wind Profiler Data Versus Time for 1 August 1990, 01:03 to 12:03 UCT.

The wind profiler is a Doppler radar designed for sensitivity to back-scattered signals from small density discontinuities present in clear air. The operating principle and Doppler effect are similar to that described for the sodar in Section 2.1, but propagation speed is the speed of light rather than the speed of sound. A large antenna, low noise electronics, and advanced signal processing techniques make it possible to extract very weak return signals out of the background noise. The profiler system consists of a 144-element coaxial-collinear antenna (area of 125 m²), a transmitter that provides 35 kW peak power, a low noise receiver, a processor with VME bus-based architecture, and a data display and archival system operating on a VAXstation 3100. Software algorithms are used to check data validity and convert radial wind information into profiles of wind speed and direction. Displays of wind profiles, returned power, and spectral width are currently available. Additional displays of wind shear, range wind, and crosswind are under development. This section describes the methodology being used to evaluate radar wind profiler performance and optimize its operation.

To optimize profiler performance, radar operation settings have been configured to produce two sets of three beams of low mode data, essentially configuring the profiler to look like two collocated 3-beam profilers. This redundancy permits direct wind reading intercomparisons at each range gate. Analysis of returned power, noise, and spectral width indicates problem areas that can be corrected through successive adjustments of profiler operating parameters to achieve a maximum signal-to-noise ratio (SNR) while obtaining measurements over the desired range of velocities and heights, and with the necessary range and velocity resolutions.

2.4.2. The Radar Equations

The ratio of received signal to background noise S_r/S_n , or SNR, is a function of transmitted power P_t and antenna characteristics, the ratio of pulse length τ to range R , a noise term, spectral width, atmospheric reflectivity η , and the product of coherent and incoherent averaging $n_c \bar{n}_i$. The SNR equation applicable to clear air radars, with related characteristics grouped within brackets, is

$$\text{SNR} = \overset{(a)}{[P_t A_e \alpha^2]} \overset{(b)}{[C \tau^2 / 16 \sqrt{2} \pi R^2]} \overset{(c)}{[\eta / \{k(T_s + \alpha T_c)\}]} \overset{(d)}{[n_c \sqrt{\bar{n}_i}]} \overset{(e)}{[m/n_g]} \quad (35)$$

Bracket (a) contains transmitted power and antenna characteristics, including the antenna loss figure α which is squared because the signal has to pass through the antenna twice. Bracket (b) contains τ , R , and constants, including the speed of light, C . Bracket (c) is the ratio of reflectivity to the noise term, which contains receiver noise T_s , cosmic noise T_c , and the Boltzmann constant k . Brackets (d) and (e) contain respectively the coherent-incoherent averaging product and the spectral width. Most of the terms in Equation (35) are fixed or are defined by the antenna, electronics, and operating frequency. Variables affecting SNR that require operator adjustment are τ , coherent averaging time, the incoherent averaging time or scan rate, and the pulse repetition period.

Pulse length τ , a squared term in Equation (35), increases SNR at the expense of range resolution. The speed of light is approximately $150 \text{ m } \mu\text{s}^{-1}$. The DPG profiler uses a pulse length of $1.67 \text{ } \mu\text{s}$ to achieve 250-m range resolution over heights ranging from 500 m to 10 km above ground level, and a $6.67 \text{ } \mu\text{s}$ pulse to achieve a 1000-m range resolution at higher altitudes. These pulse lengths are fixed, although the operator can choose to configure the system to operate on low mode ($1.67 \text{ } \mu\text{s}$), high mode ($6.67 \text{ } \mu\text{s}$), or with a combination of modes. The DPG profiler is primarily operated on low mode to achieve maximum range resolution.

The choice of $n_c \sqrt{n_i}$ strongly influences SNR and several other measured variables. Time domain averaging is determined by n_c , the number of coherent averages obtained during a sampling period, and the pulse repetition period (PRP). Maximizing time domain averaging is beneficial because return signals add constructively, while random noise signals average towards zero. Maximizing n_c therefore increases the return signal while suppressing noise. However, this averaging is based on the assumption that successive pulses strike the same scattering phenomenon. The translation and evolution of eddies within the scattering medium limit n_c . If n_c is chosen to be too large, an undesirable broadening of the signal (spectral broadening) occurs. Consequently, time domain averaging is restricted to a maximum of several seconds. The variable n_i determines the incoherent averaging time, or scan rate. Because it enters Equation (35) as a square root, n_i is less effective than n_c in increasing SNR. However, choosing a long n_i does not cause spectral broadening, so incoherent averaging time is limited principally by the need to switch beam positions. A scan rate on the order of 1 per minute is typical.

For a Doppler radar, the choice of n_c affects the full scale unambiguous radial velocity v_D and velocity resolution Δv in addition to SNR. The maximum unambiguous full scale velocity is related to the full scale Doppler frequency shift (F_D) by

$$F_D = 2v_D f_c / C \quad , \quad (36)$$

where f_c is the center frequency (404.37 MHz). The full scale radial velocity must be set large enough to sample expected wind speeds, but must be kept as small as possible to provide a reasonable velocity resolution. A V_D of 28.7, which would accommodate horizontal wind speeds in excess of 100 m s^{-1} , was chosen for the off-vertical beams, and a V_D of 17.7 m s^{-1} was chosen for the vertical beam. The result is an F_D of 77 Hz for the off-vertical beams and 47.7 Hz for the vertical beam.

Full scale frequency and the PRP define the number of coherent time domain averages as

$$n_c = 1/(2\text{PRP}F_D) \quad . \quad (37)$$

The PRP is fixed at $100 \text{ } \mu\text{s}$. Each off-vertical beam, with an F_D of 77 Hz, has an n_c of 64. The vertical beam, with its F_D of 47.7 Hz, has an n_c of 104. If

a 256-point Fast Fourier Transform (FFT) is used to transform the data, the coherent averaging time T_c becomes

$$T_c = 256n_c \text{PRP} \quad (38)$$

The resultant averaging times are 1.6 s for the off-vertical beams and 2.7 s for the vertical beam. The auto-correlation function (R_τ), or persistence of the scattering medium, is approximated by (Battan, 1959)

$$R_\tau \approx .00171 \lambda \quad (39)$$

where the wavelength (λ) is 74 cm. The constant in Equation (39) is inversely proportional to the wind velocity standard deviation, which is assumed to be 1 m s^{-1} for present computations. For a 74-cm radar, R_τ is approximately 0.13 s. Battan (1959) recommends coherent averaging on the order of $10 R_\tau$, so the T_c selected for the off-vertical axes is nearly optimum and the T_c for the vertical axis may be somewhat large. Further work is needed to determine if the vertical velocity T_c is causing excessive spectral broadening. With the currently selected settings and 1-min incoherent averaging, the $n\sqrt{n}$ product is 379 for the off-vertical axes and 488 for the vertical axis, which should optimize the SNR for the maximum number of valid returns and height ranging.

The choice of coherent averaging time affects the Doppler velocity resolution Δv according to

$$\Delta v = \lambda / 2T_c \quad (40)$$

The T_c of 1.6 s provides a horizontal velocity resolution of 23 cm s^{-1} , and the T_c of 2.7 s provides a vertical velocity resolution of 14 cm s^{-1} . These velocity resolutions contribute to the overall accuracy of profiler wind measurements. Other accuracy considerations include the spread of the velocities of the scatterers within the illuminated volume, turbulence spectrum, trends in the wind field, and presence of wind shear zones. Further studies will be needed to evaluate the combined effects of these factors on radar wind profiler performance.

2.4.3. Performance Evaluation

With profiler operating parameters set as discussed in Section 2.4.2, an initial intra-profiler evaluation was performed using the profiler's 5-beam capability. Profiler output variables consisted of easting, northing, and vertical components of the wind (u, v, w), returned power (P_x, P_y, P_z), spectral widths (xw, yw, zw), and noise levels (xnl, ynl, znl). The profiler was configured to operate in the low mode (with 250-m range resolution) as two collocated 3-beam profilers, providing an opportunity to compare complementary sets of data (east versus west beam, etc.) for case analysis. The profiler also provided vertical velocity measurements from both the x and y antenna sub-arrays that permitted a cross antenna (x-array versus y-array) evaluation of vertical velocities.

A total of 160 hourly profiler consensus data sets were collected over a 10-day period in July 1990 for case analysis. Using the dual 3-beam mode, paired measurements of each output variable were recorded at each range gate, with 28 possible range gates for each hour. The calculated differences between paired measurements, averaged over all range gates, were used for case analysis. The cases included the differences Δu , Δv , Δw , ΔP_x , ΔP_y , ΔP_z , Δx_w , Δy_w , Δz_w , Δx_{nl} , Δy_{nl} , and Δz_{nl} . The means and standard deviations calculated for each set of 160 samples were used in a statistical evaluation of the significance of the means. The null hypothesis was that the case mean (Δu , etc.) was equal to zero. This hypothesis was evaluated using a Student's t test with N-1 degrees of freedom.

2.4.4. Results

The means of Δu , Δv , and Δw were 0.045, -0.040, and -0.007 m s⁻¹, respectively. These means were not found to be significantly different from zero, indicating that the mean wind component data from the profiler's complementary beams were essentially identical. However, significant differences were found in returned power between the east-west and north-south beams. These were accompanied by significant differences in spectral widths and noise levels. This information was provided to the contractor, and some new antenna elements were installed on a subsequent site visit. Significant differences in returned power were also observed between the x- and y-array vertical beams, with a mean difference of nearly 2 dB. A possible physical explanation for the difference is that, because the y-array overlays the x-array, the signal transmitted by the x-array must pass through the y-array with a loss of power on both the outward and return trips. Another possible explanation is that an optimum distance exists between the antenna and the ground plane. Because of their physical size, both the x-array and y-array cannot be at this optimum distance from the ground plane.

Initial examination of the wind component data revealed a considerable amount of scatter in the measurements nearest the surface. This scatter, which was largely absent from layers above the boundary layer, is likely due to the large diurnal trend in the boundary layer winds and possible terrain influences from Granite Mountain. Low-level profiler winds require special scrutiny because of the relatively large inter-profiler differences. Otherwise, with the exception of cases where the SNR is low, dual beam agreement was quite good. Additional work is needed to screen the dubious data (low SNR) cases. Discrepant wind reports were most often associated with erroneous vertical velocities. Consequently, an automated procedure is needed to evaluate vertical velocities before they are used in horizontal wind computations.

2.4.5. Conclusions

The radar wind profiler exhibits great promise for providing detailed, high quality wind information on a continuous basis for test support at DPG. Questions concerning boundary layer winds and the use of vertical velocities in horizontal wind computations must be resolved in order to optimize profiler performance. Profiler evaluations will continue, with participation from the University of Utah Meteorology Department and the National Weather Service Western Region Headquarters.

INTENTIONALLY BLANK

SECTION 3. APPENDICES

APPENDIX A.
METHODOLOGY INVESTIGATION PROPOSAL AND DIRECTIVE

FY90 METHODOLOGY INVESTIGATION PROPOSAL

1. TITLE. Calibration and QC for New Met Instruments, Part III.
2. INSTALLATION/FIELD OPERATING ACTIVITY. U.S. Army Dugway Proving Ground, Dugway, UT 84022-5000.
3. PRINCIPAL INVESTIGATOR. Mr. Christopher A. Biltoft
Meteorology Division
STEDP-MT-M
Autovon 789-5101
<gross@dpg-mt.arpa>
4. BACKGROUND. DPG will acquire a 5-beam continuous atmospheric radar wind profiler (CAP) during FY89. The CAP will measure wind profiles from 500 m to 12 km and will be used for direct support of artillery programs.
5. PROBLEM. The CAP algorithms currently available are designed for 3-beam systems used for synoptic weather and aviation applications. New algorithms are needed for artillery support, quality control, and archival in the DPG archival formats.
6. OBJECTIVE. Develop internal consistency, quality control, and archival algorithms for the DPG 5-beam CAP.
7. MISSION AREA SUPPORTED. The CAP will support artillery range testing (fire support).
8. PROCEDURES.
 - a. Perform CAP performance verification using intercomparison with radiosonde flights (January 1990).
 - b. Develop range wind, crosswind, and shear algorithms for real-time monitoring of winds during artillery tests. Develop flags for out-of-tolerance conditions (March 1990).
 - c. Develop divergence algorithms for checking internal consistency of the 5-beam profiler winds. Develop standards and flags for out-of-tolerance conditions (July 1990).
 - d. Configure CAP data for data analysis, archival, and merging into report formats (August 1990).
 - e. Coordinate procedures for the exchange of CAP data with other users (September 1990).

9. JUSTIFICATION/IMPACT. CAP technology has recently become commercially available and is likely to replace radiosondes as the major source of upper level wind data in the 1990s. CAPs currently in service or planned as part of the National Network are designed for general aviation and meteorological applications. The continuous remote wind profiling capability of a CAP also makes this instrument ideal for artillery applications, but algorithms must be designed for this purpose. If not funded, the currently available CAP data will be available for weather analysis and forecasting support only. The decision to purchase a CAP was based partly on projected savings of radiosonde flight equipment used for test support. The \$200K cost of the CAP can be recovered in approximately 5 years, but only if the CAP data are available in appropriate formats.

10. DOLLAR SAVINGS. The cost of the \$200K CAP can be recovered in savings of expendable radiosonde flight equipment (approximately \$200/flight) within 5 years (200 flights/year) if the appropriate CAP software is developed. The savings of at least \$40K per year is expected to continue for the foreseeable future.

11. RESOURCES.

a. Financial.

	Dollars (Thousands) FY90	
	In-House	Out-of-House
Personnel Compensation	19.0	0.0
Materials and Supplies	1.0	0.0
Subtotals	20.0	0.0
FY Total		20.0

b. Explanation of Cost Categories.

(1) Personnel Compensation. Compensation for federal civilian employees assigned to the methodology investigation.

(2) Contractual Support. None.

c. Obligation Plan.

FQ	1	2	3	4	Total
Obligation Rate (Thousands)	5	7	5	3	20

d. Man-Hours Required. Approximately 850 in-house direct labor hours will be required to complete this investigation.

12. ASSOCIATION WITH TOP PROGRAM.

a. No TOPs will be revised as a result of this investigation.

b. No new TOPs are contemplated.

13. AUTHENTICATION.



DEPARTMENT OF THE ARMY
HEADQUARTERS, U.S. ARMY TEST AND EVALUATION COMMAND
ABERDEEN PROVING GROUND, MARYLAND 21005-5055



REPLY TO
ATTENTION OF

AMSTE-TC-M (70-10p)

20 DEC 1989

MEMORANDUM FOR: Commander, U.S. Army Dugway Proving Ground,
ATTN: STEDP-MT-A, Dugway, UT 84022-5202

SUBJECT: Amendment 2 to FY 90 RDTE Methodology Improvement
Program Grant

1. Reference Memo, HQ TECOM, AMSTE-TC-M, 2 Oct 89, subject:
FY90 Methodology Improvement Program Grant.
2. This Memo, with list of investigations at enclosure 1,
amends reference 1.
3. Point of contact at this headquarters is Ms. Cynthia
McMullen, AMSTE-TC-M, amstetcm@apg-emh4.apg.army.mil, AUTOVON
298-2170/3677.

FOR THE COMMANDER:

Encl

GROVER H. SHELTON
Chief, Meth Imprv Div
Directorate for Technology

DUGWAY PROVING GROUND		INITIAL FUNDING	REVISED FUNDING
7-CO-R90-DPO-001	QUICK REACTION METHODOLOGY	13.0	13.0
7-CO-R90-DPO-002	TECHICAL COMMITTEE SUPPORT	4.0	4.0
7-CO-R90-DPO-003	CHEMICAL ASSAY METHODS	60.0	60.0
7-CO-R90-DPO-004	CALIBRATION AND QC FOR NEW MET INSTRUMENTS II	20.0	20.0
7-CO-R90-DPO-005	USE OF AI/EXP SYS IN SMOKE DATA REDUCTION	40.0	40.0
7-CO-R90-DPO-006	HYBRIDOMA/COXIELLA BURNETII II	38.0	38.0
7-CO-R90-DPO-007	TEST SAMPLING SUPPORT	34.0	34.0
7-CO-R90-DPO-008	AEROSOL INSTRUMENTATION CHARACTERIZATION II	35.0	35.0
7-CO-R90-DPO-009	TRANSPORT & DISPERSION MODEL HIERARCHY III	25.0	25.0
7-CO-R90-DPO-010	NUMERICAL MODELING OF TEST GRID WIND IV	25.0	25.0
7-CO-R90-DPO-011	TOP FOR MULTISPECTRAL OBSCURANT TESTING	33.0	15.0
7-CO-R90-DPO-012	REAEROSOLIZATION OF BIO HAZARDS-CRDEC		
7-CO-R90-DPO-013	AEROSOL PENETRATION OF FABRICS	0.0	18.0
		----	----
	TOTAL DPG PROGRAM	327.0	327.0

APPENDIX B. REFERENCES

- Battan, L. J., 1959: Radar Observation of the Atmosphere. U. of Chicago Press, Chicago, 324 pp.
- Biltoft, C. A., 1987: Development of sonic anemometer software. DPG-FR-88-702 (AD#B120769), U.S. Army Dugway Proving Ground.
- Biltoft, C. A., 1988: Field test of a crosswind scintillometer. DPG-FR-88-317 (AD#A200697), U.S. Army Dugway Proving Ground.
- Brooks, C. E. P., and N. Carruthers, 1953: Handbook of Statistical Methods in Meteorology, London, Her Majesty's Stationary Office, 412 pp.
- Engineering Design Handbook, DARCOM-P 706-103. Selected topics in experimental statistics with Army applications. U.S. Army Materiel Development and Readiness Command. December 1983.
- Fand, R. M., and K. K. Keswani, 1972: A continuous correlation equation for heat transfer from cylinders to air in crossflow for Reynolds numbers from 10^{-2} to 2×10^5 . Int'l J. of Heat and Mass Transfer, 15, 559-562.
- Fuchs, M., and C. B. Tanner, 1965: Radiation shields for air temperature thermometers. J. Appl. Meteor., 4, 544-547.
- Greenberg, S. A., D. A. Vance, and E. R. Streed, 1967: Low solar absorptance surfaces with controlled emittance: A second generation of thermal control coatings. In Prog. Astron. Aeron., Academic Press, 20, 297-309.
- Grubbs, F. E., 1948: On estimating precision of measuring instruments and product variability. J. Amer. Statistical Assn., 43, 243-264.
- Grubbs, F. E., 1973: Errors of measurement, precision, accuracy and the statistical comparison of measuring instruments. Technometrics, 15, 53-66.
- Grum, F. and G. W. Luckey, 1968: Optical sphere paint and a working standard of reflectance. Appl. Opt., 7, 2289-94.
- Kaimal, J. C., and J. E. Gaynor, 1983: The Boulder Atmospheric Observatory. J. Clim. and Appl. Meteor., 22, 863-880.
- Kondratyev, K. Y., 1969: Radiation In The Atmosphere. Academic Press, NY, 912pp.
- Lee, R. W., 1974: Remote probing using spatially filtered apertures. J. Opt. Soc. Amer., 64, 1295-1303.
- Luers, J. K., 1990: Estimating the temperature error of the radiosonde under different environments (manuscript submitted to J. Atmos. Oceanic Tech).

- Morgan, D. L., W. O. Pruitt, and F. J. Lourence, 1970: Radiation data and analysis for the 1966 and 1967 micrometeorological field runs at Davis, California. ECOM 68-G10-2, University of California, Davis (AD702-236).
- Ochs, G. R., J. J. Wilson, S. Abbott, and R. George, 1988: Crosswind profiler Model II. NOAA Technical Memorandum ERL/WPL 152.
- Palmer, T. R., and E. M. Hansen, 1956: An investigation of ultraviolet and solar intensity at Dugway Proving Ground for the months of July through December, 1955. Unpublished technical report, Meteorology Division, Materiel Test Directorate, Dugway Proving Ground, UT.
- Thompson, W. A., 1963: Precision of simultaneous measurement procedures. J. Amer. Statistical Assn., 58, 475-479.
- Touloukian, Y. S., D. P. DeWitt, and R. S. Hernicz, 1972: Thermophysical Properties of Matter, Volume 9, Thermal Radiative Properties, Coatings. IFI/Plenum, N.Y.